Modification of Oxide Surfaces with Functional Organic Molecules, Nanoparticles, and Hetero-Oxide Layers

Chaudhary, Shilpi

2015

Modification of Oxide Surfaces with Functional Organic Molecules, Nanoparticles, and Hetero-Oxide Layers

Shilpi Chaudhary

Division of Synchrotron Radiation Research

LUND
UNIVERSITY

DOCTORAL DISSERTATION

Division of Synchrotron Radiation Research
Department of Physics
Lund University
ISBN: 978-91-7623-329-0 (Print)
978-91-7623-330-6 (Pdf)

Printed in Sweden by Media-Tryck, Lund University
Lund, June 2015


"We are shaped by our thoughts; we become what we think. When the mind is pure, joy follows like a shadow that never leaves."

Buddha

"If we knew what it was we were doing, it would not be called 'research', would it?

Albert Einstein

Abstract

The research work described in this thesis is concerned with the modification of oxide surfaces, as reflected by its title. The surfaces and their modification have been studied using a range of experimental surface characterization tools, in particular x-ray photoelectron spectroscopy (XPS), fluorescence microscopy, scanning electron microscopy, atomic force microscopy, and scanning tunneling microscopy.

A large part of the thesis is related to the modification of oxide or metal surfaces with nanoparticles. In particular, three different immobilization schemes for the coupling of molecularly imprinted polymer (MIP) nanoparticles to silicon oxide (SiO_2) and gold surfaces were designed and characterized at every step. The first method reports the immobilization of MIPs using a photo-coupling agent in combination with an aminosilane compound. The second method explores an epoxysilane-based coupling agent to directly anchor the nucleophilic core-shell MIP nanoparticle to the surface. Both methods were proven to be non-destructive towards the specific binding sites of the MIP nanoparticles. The third scheme offers the immobilization of nucleophilic core-shell nanoparticles on model gold surfaces using self-assembled monolayers of 11-mercaptoundecanoic acid activated by carbodiimide/N-hydroxysuccinimide. All three coupling methods are quite versatile and can be used in biosensors to couple functional nano-objects with transducer surfaces. In addition to these investigation directly aimed at the immobilization of nanopartciles, more fundamentally oriented studies were carried out on the modification of the rutile TiO_2(110) surface with silane molecules to obtain a detailed understanding of adsorption mechanism and geometry of these silanes.

The deposition of a different type of nanopartciles, block copolymer reverse micelles loaded gold nanoparticles, on a titanium dioxide surface was tested using electrospray deposition. The study demonstrates that electrospray deposition is a viable method for depositing metal single-size metal nanoparticles onto a surface in vacuum, thereby retaining the clean vacuum conditions. Furthermore, it was shown that the removal of the block copolymer shell after deposition can be achieved both by atomic oxygen and an oxygen plasma, with the atomic oxygen being somewhat more efficient. Overall, it was demonstrated that a TiO_2 surface decorated with narrow sized gold nanoparticles could be created, a result of importance in the catalysis domain.

The last part of the thesis is concerned with the true *in-situ* investigation of growth of hetero-oxide layers on oxide surfaces from metal precursors. Tetraethyl orthosilicate (TEOS) was used as precursor for the chemical vapor deposition of silicon oxide on rutile TiO_2(110). The growth was monitored in real time using ambient pressure XPS (APXPS), which revealed the dissociative adsorption with the formation of new species in the presence of a TEOS gas phase reservoir. Annealing results in the formation of SiO_2 and of a mixed titanium/silicon oxide. Furthermore, tetrakis(dimethylamino)titanium was employed in the atomic layer deposition (ALD) of TiO_2 on RuO_2. The APXPS results showed evidence was for side reactions beyond the idealized scheme of ALD.

Contents

Contents 5

Popular Science Summary 6

List of Papers 8

1. Introduction and Motivation 10
   - 1.1 Immobilization of nano-objects 10
   - 1.2 Oxide-oxide interfaces 13

2. Experimental Techniques 14
   - 2.1 X-ray Photoelectron Spectroscopy 14
     - 2.1.1 Principle and Theory 14
     - 2.1.2 Instrumentation for X-ray Photoelectron Spectroscopy 19
     - 2.1.3 Analysis of Photoemission Spectra 21
   - 2.2 Ambient Pressure X-ray Photoelectron Spectroscopy (APXPS) 23
   - 2.3 Scanning Tunneling Microscopy 25
     - 2.3.1 Principle and Theory 25
     - 2.3.2 Instrumentation for STM 27
   - 2.4 Other Techniques 28

3. Materials and Methods 31
   - 3.1 Materials 31
     - 3.1.1 Molecules 31
     - 3.1.2 Nanoparticles 32
     - 3.1.3 Substrates 33
   - 3.2 Methods 34

4. Results 35
   - 4.1 Immobilization of MIP Nanoparticles on SiO_2 and Gold 35
   - 4.2 Adsorption of Silane Molecules on the Rutile TiO_2(110) Surface 40
   - 4.3 Gold-loaded Block Copolymer Reverse Micelles on the Rutile TiO_2(110) Surface 41
   - 4.4 Growth of Silicon Oxide on the Rutile TiO_2(110) Surface 42
   - 4.5 Growth of TiO_2 on the RuO_2(110) surface 43

5. Summary and Future Outlook 45

Acknowledgement 47

References 49

Popular Science Summary

It is hard to imagine present day's lifestyle without the use of modern technologies as prevalent in sectors including bioscience & technology and the semiconductor & chemical industries. In technological advances of biosensors, catalysis, and microelectronics, the surface modification of materials (which includes modification of the wetting, structural, electrical, mechanical properties etc.,) is required. Generally, the surface of a material is defined as the boundary layer between the solid and a gas, vacuum, or liquid phase and it has physical and chemical properties significantly different from the bulk of the material. At the same time many of the surface properties are decisive for how the material behaves in an application. This makes the surfaces of a material particularly interesting for detailed investigations, including the question of how one can deliberately modify their properties. This thesis mainly explores the modification of oxide surfaces with organic molecules and nanoparticles in view of their manifold applications in biosensors, catalysis, and microelectronics.

Often, in case of biosensors, organic molecules are used to couple functional nano-objects with the surface of transducers – a device, which converts one form of energy (in this case an electrical signal) into a measurable form. Here, different immobilization methods were designed and characterized to anchor molecularly imprinted polymers (MIPs) with model supports, e.g., silicon oxide and gold surfaces. MIPs are artificial template made receptors based on the "key-lock" mechanism, where MIPs act as a lock with the template being their key. In this thesis, the template (key) of choice was propranolol, which.is a drug for reducing hypertension, migraine headaches, and high blood pressure. The methods used to firmly anchor the MIPs were proven to be non-destructive towards the template's binding sites. The coupling methods used in this thesis are fairly versatile to anchor functional nano-objects and can be considered as an initial step towards the formation of working nanosensors. Further, the detailed investigations of these anchoring organic molecules resulted in understanding how they sit on oxide surfaces with respect to their functional groups.

Catalysis uses external substances to make chemical reactions easier and is a very important process in the chemical industry. The conversion of carbon monoxide (CO – a highly poisonous gas for humankind) to a non-poisonous gas, carbon dioxide (CO_2), is one of the crucial issues in the automobile industry. The integration of well-distributed small gold nanoparticles with oxide surfaces results in catalysts materials with a high catalytic activity for the conversion of CO into CO_2 at or even below room temperature. However, gold nanoparticles have the major drawback of forming big clusters by combination of nearby nanoparticles at high temperatures, thus killing the catalytic properties. This

problem can be solved by surface modification or by using molecular spacers to prevent particle combination. A method has been designed for surface deposited gold nanoparticles with narrow size distribution and presented in this thesis.

Flexible devices are new amazing tools in the semiconductor technology for electronics and telecommunication industry, which requires the ultimate miniaturization of devices. This miniaturization demands new methods to control the fabrication processes at very small scales on the order of the microlevel. Chemical vapor deposition (CVD) and atomic layer deposition (ALD) are promising microfabrication methods to grow high quality thin films with uniform thickness and surfaces. In recent years, thin films have proven their potential in the fabrication of commercially available flexible displays. Both methods involve a chemical reaction of a volatile precursor (parent unit) of the desired material to be deposited on the surface of a substrate and to react there to form the desired thin film. In ALD in then a second reaction step is required with a second volatile parent unit. As part of this thesis, the mechanism of both thin film deposition methods has been investigated for the growth of silicon oxide on titanium dioxide and titanium dioxide on ruthenium dioxide in real-time. The oxide layers grown during the course of this thesis have potential to serve as insulating layers, dielectrics, in microelectronic devices. The investigations of thin film deposition presented in this thesis may help to understand the surface chemistry of these processes to produce the desirable quality of thin films for industrial uses.

List of Papers

This thesis is based on papers **1-8**. I was main responsible for carrying out the experiments, analysis of the data, and writing the manuscripts in the cases of papers **1, 4, 5** and **7**. I took part in the spectroscopy experiments, analysis of data, discussions of results, and writing of the manuscript in the case of **papers 2, 3, 6,** and **8**.

Paper 1

S. Chaudhary, T. Kamra, K. M. A. Uddin, O. Snezhkova, H. S. N. Jayawardena, M. Yan, L. Montelius, J. Schnadt, and L. Ye, *Controlled short-linkage assembly of functional nano-objects*

Applied Surface Science **300**, 22 (2014).

Paper 2

T. Kamra, S. Chaudhary, C. Xu, N. Johansson, L. Montelius, J. Schnadt, L. Ye, *Covalent mmobilization of molecularly imprinted polymer nanoparticles using an epoxy silane*

Journal of Colloid and Interface Science **445**, 277 (2015).

Paper 3

T. Kamra, S. Chaudhary, C. Xu, L. Montelius, J. Schnadt, L. Ye, *Covalent Immobilization of Molecularly Imprinted Polymer Nanoparticles on a Gold Surface using Carbodiimide Coupling*

Submitted to Journal of Colloid and Interface Science.

Paper 4

S. Chaudhary, R. Sánchez-de-Armas, A. R. Head, N. Johansson, O. Snezhkova, T. Kamra, L. Montelius, L. Ye, *F.* Bournel, J.-J. Gallet, B. Brena, J. Schnadt, *Synchrotron-based XPS studies of adsorption of (3-aminopropyl)triethoxysilane on rutile TiO_2(110) in UHV and at ambient pressure*

In manuscript.

Paper 5

S. Chaudhary, A. R. Head, J. Schnadt, *X-ray photoelectron spectroscopy study of adsorption of (3-mercaptopropyl)trimethoxysilane and n-propyltriethoxysilane on a rutile TiO_2(110) surface*

Advanced Materials Letters **6**, 279 (2015).

Paper 6

A. R. Head, S. Chaudhary, M. E. Messing, F. Bacque, N. Johansson, O. Snezhkova, T. Kamra, J. N. Andersen, and J. Schnadt, *Electrospray deposition of gold-loaded block copolymer reverse micelles onto a clean TiO_2 surface in vacuum*

Submitted to Nanotechnology.

Paper 7

S. Chaudhary, A. R. Head, R. Sánchez-de-Armas, H. Tissot, G. Olivieri, F. Bournel , L. Montelius, L. Ye, F. Rochet, J.-J.Gallet, B. Brena, and J. Schnadt, *Real-Time Study of CVD Growth of Silicon Oxide on Rutile TiO_2(110) using Tetraethyl Orthosilicate.*

Submitted to Journal of Physical Chemistry C.

Paper 8

A. R. Head, S. Chaudhary, G. Olivieri, J. N. Andersen, F. Rochet, F. Bournel, J.-J. Gallet, and J. Schnadt, *Ambient pressure x-ray photoelectron spectroscopy study of the atomic layer deposition of TiO_2 on RuO_2(110)*

In manuscript.

List of papers not included in the thesis

In addition to my thesis project, I had the opportunity to participate in collaborations on different projects, which resulted in the following papers:

Paper 9

T. Zhou, X. Shen, S. Chaudhary, and L. Ye, *Molecularly imprinted polymer beads prepared by pickering emulsion polymerization for steroid recognition*

Journal of *Applied Polymer Science* **131**, 39606 (2014).

Paper 10

C. Huang, T. Kamra, S. Chaudhary, and X. Shen, *Breath figure patterns made easy*

*ACS Applied, Materials & Interface*s **6**, 5971 (2014).

1. Introduction and Motivation

Hybrid organic/inorganic materials are becoming more and more popular due to their wide range of applications in biomedical devices, molecular electronics [1,2], dye sensitized solar cells (DSSC) [3,4], nanosensors [5,6], and catalysis [7,8]. In the case of biosensors, the interaction between the recognition elements (mostly organic materials) and transducer surface (typically an oxide surface) is one of the most important aspects of sensing since it is responsible for the output of the sensing signal. In addition, recent advancements in microelectronics (e.g. metal-oxide semiconductor field-effect transistors) have been realized due to advancements in chemistry at the oxide interface; however, the details of this chemistry are still uncertain and therefore a better fundamental understanding of oxide-oxide interactions is necessary [9]. In order to accelerate the technological advancement of these fields, a clearer understanding of hybrid material interfaces is necessary. The surface science approach is the most suitable paradigm to employ in order to realize an improved fundamental understanding of chemical/physical aspects of hybrid interfaces. This thesis presents mainly two aspects of hybrid interfaces: one that involves immobilization of functional organic molecules and gold nanoparticles on oxide and metal supports, whereas the second aspect presents real-time investigations of oxide thin films on oxides supports. X-ray photoelectron spectroscopy (XPS) and microscopic techniques (fluorescence microscopy, scanning electron microscopy (SEM), atomic force microscopy (AFM), and scanning tunneling microscopy (STM) were used to investigate these hybrid interfaces.

1.1 Immobilization of nano-objects

Biomedical devices mainly consist of biorecognition elements and sensor surfaces. One of the interesting strategies in building biomedical devices is to first fabricate the recognition elements and then combine them with the sensor surface. To synthesize recognition elements, nanotechnology provides the freedom to modify the specific properties of a material to make it more reactive, stable, handy, and lighter. To combine these functional nanomaterials with the model support (such as required in the integration of biomimetic materials on the surface of sensor substrate), there is a call for reliable and well-controlled routes to the assembly of nanomaterials at desired locations. The functional materials can be attached to specific locations either directly (*in situ)* or using linker molecules (such as polymers [10]). The *in situ* attachment method cannot make full use of the optimized parameters at the time of fabrication of such nano-objects, and it also blocks the sensitive sites for recognition of templates due to loss of some part of surface area. Thus there is a

need to couple ready-made functional nano-objects to specific locations on another material. The linkage of nano-objects using a polymer involves a thick layer of polymer which, in the case of nano-object sensing, may sacrifice recognition sites. The physical distance between the functional nano-objects and their binding sites is also of utmost importance as many applications require efficient energy transfer, e.g. in the form of electrons. As model nano-objects, molecularly imprinted polymer (MIP) nanoparticles have been used in **papers 1, 2**, and **3**. MIPs are biomimetic, synthetically made receptors that are more stable and producible at low cost as compared to natural receptors, and can be used in various applications such as in artificial enzymes, chemical sensors [11,12], and drug delivery systems[13]. MIPs are obtained by polymerization of functional monomer and cross-linker in the presence of desired template molecules (see Figure 1.1), and the removal of template leaves behind cavities, which are complementary in shape and size of the template [14]. In **papers 1** and **2** the potential of short silane coupling agents to covalently couple MIP nanoparticles to glass surfaces and verification of their nondestructive nature towards the functionality of MIP nanoparticles was explored.

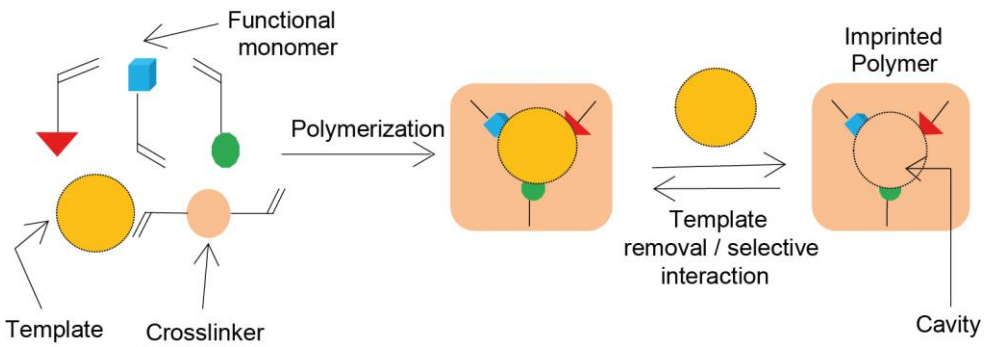

Figure 1.1. Scheme of the process of synthesizing a MIP.

In **paper 1**, aminosilane-terminated oxide surfaces were further modified with simple photoactivated conjugation chemistry to immobilize MIP nanoparticles on a model transducer surface. The silane coupling agent in combination with the photocoupling agent can be used to create a controlled short-linkage assembly between a support and the MIP particles in a way that preserves the functionality of the MIP particles. The advantage of this approach is that it removes the need for an intermediate layer, and the contact between the MIP particles and the support is immediate, a crucial advantage from a molecular sensing point of view. In **paper 2** epoxide silane chemistry was employed to immobilize the amine-coated MIP nanoparticles covalently on a flat glass surface. The method achieves a homogeneous distribution of amine-coated MIP nanoparticles, which does not sacrifice the functionality or molecular selectivity. In **paper 3**, carbodiimide-based coupling chemistry was studied at every step to anchor amine-coated MIP nanoparticles to

a model gold transducer surface. Figure 1.2 depicts these different coupling agents for immobilization of MIP nanoparticles.

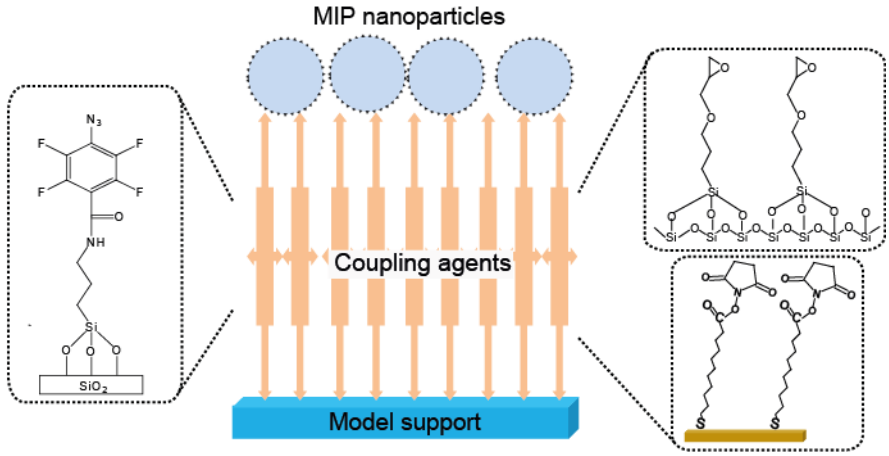

Figure 1.2. Scheme for immobilization of MIP nanoparticles using different coupling agents.

Papers 4 and **5** present a detailed investigation of adsorption of silane molecules on rutile TiO_2(110), which is an important initial step for applications involving these molecules as coupling agents. A detailed investigation may suggest reasons for formation of agglomeration and non-uniform coverage of functional molecules (as presented in Paper 1 and 2). Such findings of adsorption geometries on oxide surfaces can be used potentially to control the specific properties of surfaces and to anchor the functional nano-objects and metal nanoparticles at a molecular level.

The combination of metal nanoparticles with oxide surfaces is also a topic of great interest in both the chemical and energy industries, e.g., in heterogeneous catalysis [15,16]. The interface of small gold nanoparticles with an oxide support, in particular TiO_2, has high catalytic activity for CO oxidation at or even below room temperature [17]. One of the central issues of such a catalytic system is that the increase in temperature leads to sintering of the small gold nanoparticles, which leads to a diminishing of the catalytic activity. Thus there is an immediate demand to overcome the sintering of gold nanoparticles either by surface modification or by keeping the nanopartciles apart by spacers. Figure 1.3 shows a schematic for the steps to circumvent the agglomeration of nanoparticles via physical barriers. In **paper 6**, gold-loaded reverse micelles nanoparticles have been deposited on rutile TiO_2 (110) using electrospray deposition. An efficient way to remove the polymer shell was investigated using atomic oxygen and oxygen plasma. The deposition of TiO_2 via a molecular precursor, titanium (IV) isopropoxide, on gold-loaded reverse micelles nanoparticles could result in porous oxide TiO_2 surface with well separated gold nanoparticles and be a catalysis system for CO oxidation.

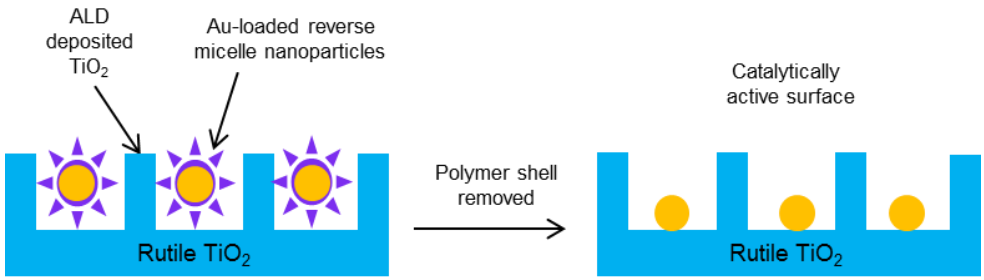

Figure 1.3. Schematic for the preparation of catalytically active porous TiO_2 surface loaded with well-separated gold nanoparticles.

1.2 Oxide-oxide interfaces

Oxide interfaces have a range of properties which makes them promising for novel electronics applications. The growth of thin oxide films on different surfaces is of utmost importance and has been widely explored in literature with various depositions methods [18,19,20,21]. Among these, chemical vapor deposition (CVD) is one of the promising methods which involve chemical processes to offer high quality of thin films with uniform coverages [22]. Alkoxysilanes are potential candidates as gaseous precursors for the CVD fabrication of silicon oxide [23] as dielectric layers [24] in the semiconductor industry and in photocatalysis [25]. An important aspect of this thesis is the detailed investigation of how silicon oxide grows on oxide surfaces at ambient conditions. In paper 7, a real-time study of CVD of silicon oxide on rutile TiO_2(110) using tetraethyl orthosilicate (TEOS) by ambient pressure x-ray photoelectron spectroscopy (APXPS) was performed.

Atomic layer deposition (ALD) is another thin film deposition method, very similar to CVD except that ALD breaks the reaction into two half-reactions [26]. Even though CVD offers high quality of thin films with uniform coverages, ALD provides precise control of layer thickness due to its, in the ideal case, self-limiting deposition mechanism with large area uniformity even on three-dimensional surfaces. Another advantage of ALD is that the deposition temperatures are significantly lower compared to those in CVD. Here a combination of TiO_2 and RuO_2 has been studied, a hetero-oxide layer combination which is of particular interest for its possible applications in dynamic random access memory [27, 28]. In paper 8, the ALD of TiO_2 on RuO_2(110) using tetrakis(dimethylamido)titanium and water was investigated with APXPS. These kinds of investigations enable the identification of surface species while a chemical reaction is ongoing. Overall, this kind of study offers an enhanced understanding of the chemical processes underlying both CVD and ALD, techniques of prominence in the semiconductor industry.

2. Experimental Techniques

This chapter describes the tools that have been used for the characterization of samples in the present thesis. These include XPS, APXPS and other material characterization techniques.

2.1 X-ray Photoelectron Spectroscopy

2.1.1 Principle and Theory

XPS is a method where x-ray light photoexcites electrons bound in atoms, molecules, or solids with a binding energy that is less than the energy of the impinging x-rays. The kinetic energy of the photoemitted electrons is then measured by an electron spectrometer. In other words, the photoelectric effect, first observed by Heinrich Hertz and later interpreted by Albert Einstein29 (he was awarded the Nobel Prize in 1921 for his interpretation), forms the basis of the method. XPS is also known as electron spectroscopy for chemical analysis (ESCA), developed to a high degree by Kai Siegbahn's research group, for which he was honored with the Nobel Prize in Physics in 1981[30].
Figure 2.1 illustrates schematically the process of photoemission for a semiconductor sample. In the photoemission process, a beam of x-rays is incident on a sample resulting in photoelectrons from core levels and valence band levels depending on the x-ray photon energy. The kinetic energy (KE) of the outgoing photoelectrons can be measured using an electron energy analyzer. The binding energy (BE) can be evaluated by applying the photoelectric equation $BE = h\nu - KE - \phi$, where $h\nu$ is the energy of the x-rays and ϕ is the work function of the sample (minimum energy required to promote an electron from the Fermi level to the vacuum level specific for the investigated surface). The binding energies of the core electrons are characteristic for each element and, moreover, depend on the chemical state of the atom. The core electrons do not participate in the chemical bonding, but different chemical states of the same atom arises due to a change in the valence electron distribution (which takes part in the bonding) causing a shift in the core level binding energies, known as a chemical shift [31]. In photoelectron spectroscopy, the chemical shifts can result from a change in the chemical environment either in the initial or final state of the system. Some of the initial state effects include the shifts due to different oxidation states and chemical bonding of atoms from which the photoemission originates. The chemical shift resulting from different oxidation states is a typical initial state effect,

whereas in general surface core level shifts have contributions both from the initial and final state [32].

The final state contributions are shake-up/shake-off satellites (intrinsic satellites) and core hole screening. In addition, extrinsic scattering (plasmons) can further modify the observed lineshapes. The binding energy of a bound electron is represented by the difference between the total final state energy (after the photoemission process) of the system consisting of N-1 electrons, E_i^{N-1}, and the total initial state energy of the system E_f^N (before the photoemission process). To arrive at this conclusion, one starts with an application of the principle of energy conservation,

$$E_i^N + h\nu = E_f^{N-1} + KE + \phi. \quad (2.1)$$

One can rewrite the above equation as

$$h\nu - KE - \phi = E_f^{N-1} - E_i^N. \quad (2.2)$$

The binding energy is determined with respect to Fermi level, so that

$$BE = h\nu - KE - \phi = E_f^{N-1} - E_i^N. \quad (2.3)$$

An electron energy analyzer is used to measure the kinetic energy KE of the emitted electron. The Fermi levels of the sample and the analyzer are aligned during the measurement because they are in electrical contact, which makes it an ideal point of reference for the case of metallic and low-bandgap semiconductor samples. In reality, the measured kinetic energy is the kinetic energy with respect to the vacuum level of the analyzer (KE'), as shown in Figure 2.1. Therefore the work function in equation 2.3 represents $\phi_{analyzer}$. KE' is different from the kinetic energy KE relative to the sample vacuum level by $\phi_{analyzer} - \phi_{sample}$. Since the binding energy is defined relative to the Fermi level this has only practical relevance: to determine the precise value of the binding energy of the sample, not only the level of interest has to be determined, but also the position of the Fermi level. The difference between the two measured kinetic energies is the binding energy.

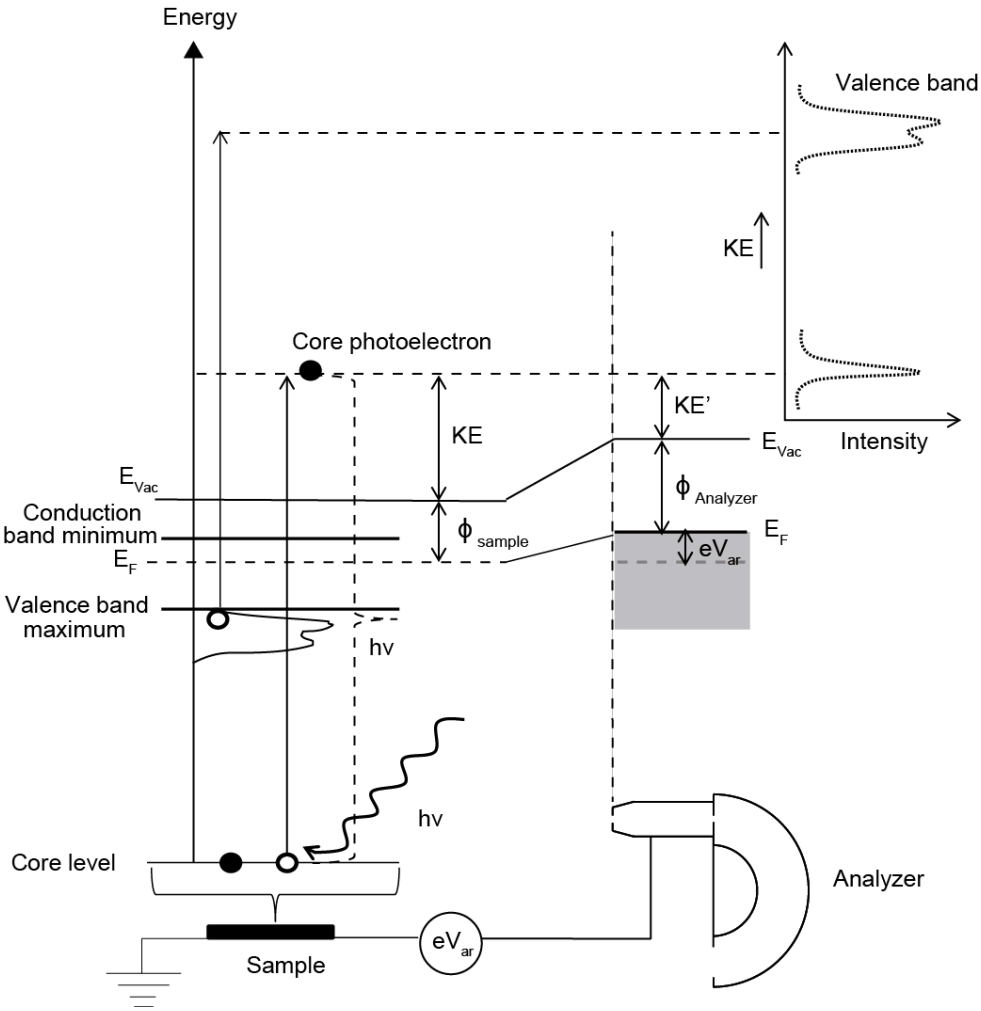

Figure 2.1. Schematic of the photoemission process, where a core electron is emitted in vacuum after interaction with a photon of sufficient energy to induce photoemission. The (here semiconducting) sample is in electrical contact with the analyzer, which results in alignment of the Fermi levels (shifted by an amount of eV_{ar}, where V_{ar} is the acceleration/retardation potential [33]). The XP spectrum shows the number of detected electrons as a function of binding energy. The sharp peak for core levels arises due to the localized nature of the core electrons. On the other hand the delocalized nature of the valence electrons gives the broad peak.

A combination of Fermi's Golden rule with the electric dipole approximation gives the transition probability per unit time between an initial state Ψ_i and final state Ψ_f. The transition probability can be written as:

$$\omega_{i\to f} \propto \frac{2\pi}{\hbar}\left|\langle\Psi_f(N)|\vec{r}|\Psi_i(N)\rangle\right|^2 \delta\left(E_f{}^{N-1} - E_i{}^{N} - h\nu\right) \qquad (2.4)$$

In equation (2.4) $\vec{r}$ is the dipole operator. The δ function assures the energy conservation in the transition. ${E_f}^{N-1}$and ${E_i}^{N}$are the final and initial state energies of system, respectively, and $h\nu$ is the energy of radiation.

For the system containing *N* electrons, the photoionization process leads to the addition of one free electron with kinetic energy (KE) to the final state of the system. To write the initial and final state wave functions for a system, one can use the "one-electron approximation". The initial state wave function can be written as a product of the one electron wave function of the orbital from which the electron was emitted ($\Phi_{i,k}$) and the many-electron wave function of the remaining electrons $\Psi_i^k(N-1)$ before photoemission. The final state wave function can be written as the product of the wave function of the emitted electron ($\Phi_{f,k}$) and the many-electron wave function of the remaining electrons $\Psi_f^k(N-1)$ after photoemission. The transition matrix elements can then be written as

$$\langle \Psi_f(N)|\vec{r}|\Psi_i\,(N)\rangle = \langle \Phi_{f,KE}|\vec{r}|\Phi_{i,k}\rangle\langle \Psi_f^k(N-1)|\Psi_i^k(N-1)\rangle. \qquad (2.5)$$

In the **frozen-orbital approximation**, the spatial distribution and energies of the (N-1) electrons remaining after photoemission are the same as in the initial state, i.e.$|\Psi_f^k(N-1)\rangle = |\Psi_i^k(N-1)\rangle$, which gives an overlap integral of unity, and therefore the transition matrix element builds just upon the one-electron wave functions. Within the frozen orbital approximation the binding energy is equal to the negative of the Hartree–Fock orbital energy of the orbital from which the electron emission took place. This is known as Koopmans' theorem.

According to the **sudden approximation**, the x-ray excited photoemission is instantaneous (in reality its time length is in the range of approximately ten attoseconds) with respect to relaxation processes, i.e. the valence electrons do not have time to respond to the change of the core hole potential. The sudden approximation allows multiple final states [34] with the same core hole. The wave function $\Psi_f^k(N-1)$ is not an eigenstate of the final state Hamiltonian, but it can be written as a sequence of eigenstates with corresponding eigenvalues, i.e. the final state with (N-1) electrons has *s* excited states with the wave function $\Psi_{f,s}^k(N-1)$. Now, the transition matrix element must be estimated by summing over the overlap integral for all possible excited final states:

$$\langle \Psi_f(N)|\vec{r}|\Psi_i\,(N)\rangle = \langle \Phi_{f,KE}|\vec{r}|\Phi_{i,k}\rangle \sum_s \langle \Psi_{f,s}^k(N-1)|\Psi_i^k(N-1)\rangle. \qquad (2.6)$$

According to equation (2.6) the photoemission spectrum includes the main line (corresponding to the most relaxed state) and features at the high binding energy side known as shake-up/shake-off satellites lines. The intensity of the main line and shake-up/shake-off satellites depends on the overlap integral between the initial and final states of the wave function. Further satellite features may occur, which may be cast in quite much the same picture. These are due charge transfer and/or polarization screening, phonons, and in the case of metallic samples an asymmetry towards the high binding energy side of the main peak due to non-quantized shake-up-like excitations at the Fermi

level. These satellite features can be categorized into intrinsic and extrinsic parts (on the basis of the *three step* model[1]). The features that arise in the actual photoemission process are termed intrinsic losses (or intrinsic satellites) whereas the extrinsic part arises due to inelastic scattering during the transfer of a photoelectron to the surface [31].

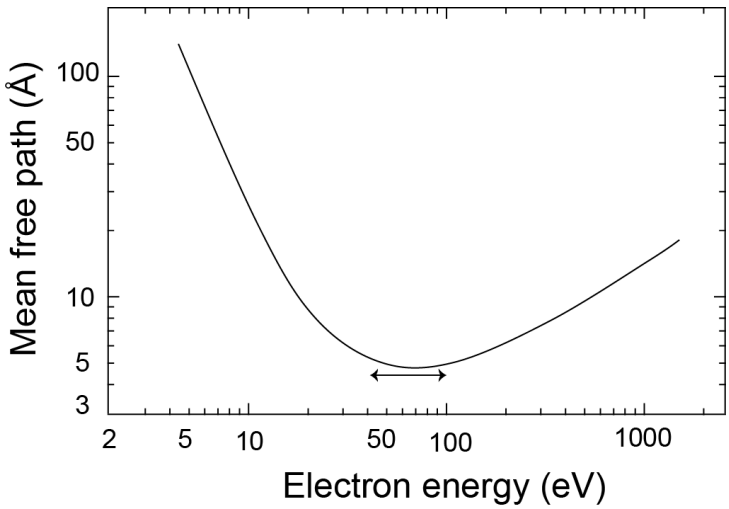

Figure 2.2. The universal curve of surface science representing the electron inelastic mean free path variation as a function of kinetic energy with a minimum (shown with double arrow) at around 50-100 eV. This figure is redrawn from Ref. [35].

While the x-ray penetration depth for materials lies in the range of microns, the escape length of electrons is on the scale of Ångströms (Å) to nanometers (nm). Since in XPS electrons are measured, it is therefore a surface sensitive technique. The distance an electron can travel within a material before it loses its energy in an inelastic scattering process is termed the inelastic mean free path (IMFP). In fact, the attenuation length is the more relevant quantity as a measure of surface sensitivity because it also accounts for the elastic scattering contribution. The average distance travelled by the electrons will decrease due to elastic scattering, which increases the probability of inelastic losses [36]. Typically the attenuation length is ~10 % smaller than the IMFP [37]. The electron IMFP of a material has a strong dependence on its kinetic energy. The curve for the electron IMFP as a function of its kinetic energy is represented in Figure 2.2 and is known as the "universal curve of surface science". The minimum of this curve (at ~50-100 eV)

[1]The three step model divides the photoemission process into three steps: (i) excitation of the photoelectron, (ii) travel of the photoelectron to the surface, and (iii) escape of the photoelectron into the vacuum.

corresponds to maximum surface sensitivity (~5-10 Å). The IMFP is also a characteristic property of each material, since it is mainly determined by electron-electron collisions that depend on a material's specific properties such as the dielectric constant. The electrons in many materials can approximately be assumed to act as a free electron gas, where the IMFP is given by mean of electron-electron distance which is approximately the same for all materials[31] and therefore the IMFP curve is nevertheless quite universal.

2.1.2 Instrumentation for X-ray Photoelectron Spectroscopy

Any setup for x-ray photoelectron spectroscopy consists of an x-ray source, an electron energy analyzer, and a high vacuum environment. The x-ray source is of course an indispensable component in photoemission spectroscopy. The sources can be divided into two categories, namely, lab sources and synchrotron radiation-based sources.

The lab source includes an anode and cathode. The electrons generated by the hot cathode are accelerated towards the anode (a metal target) by applying a high voltage between the cathode and anode. These electrons interact with the material and lead to emission of inner-shell electrons, leaving behind a hole. This hole is filled by an outer level electron with a loss of energy emitted as an x-ray photon. The x-ray emission energies are characteristic for different materials. Frequently, magnesium and aluminum metals are used for lab sources which produce photons of energies 1253.6 and 1486.6 eV, respectively. Lab sources are relatively economical and portable, but they have low flux, their energy cannot be tuned, and they have low resolution compared to synchrotron radiation-based sources.

Synchrotron radiation is created when relativistic electrons are deflected from their straight trajectories. A typical synchrotron radiation source broadly consists of an electron source (electron gun), accelerators, vacuum systems, storage ring, and beam lines. The beam lines are set up tangentially to the storage ring. Beam lines mainly consist of the monochromator, adjustable slits and baffles and focusing and collimating mirrors. The experimental end stations are built at the end of beam lines. Both lab sources and synchrotron radiation-based sources have been used for spectroscopy measurements presented in this thesis.

The electron energy analyzer is the main part of the spectroscopic instrumentation for XPS and measures the kinetic energy distribution of photoelectrons emitted upon x-ray exposure. Hemispherical electron energy analyzers are used for XPS measurements in the present thesis (depicted in Figure 2.3). They consist of an electrostatic lens arrangement, two concentric hemispheres held at a constant potential difference, a microchannel plate (MCP) detector, phosphorous screen, and charge-coupled device (CCD) camera. The photoelectrons are emitted in all directions as a result of the interaction of the sample with photons of sufficient energy. Only a fraction of them are captured by the analyzer, which is

governed by the acceptance angle of analyzer. The photoelectrons of sufficient energy enter the electrostatic lens system, which focuses them onto the entrance slit of the hemispherical analyzer and either retards or accelerates the kinetic energy of electrons depending upon the chosen pass energy E_{pass}. The photoelectrons then pass through the entrance slit and enter the space between the concentric hemispheres, where the inner sphere has a positive potential (+V) and the outer sphere a negative (-V) potential relative to the electron kinetic energy to be measured. The electron trajectories bend differently according to the electrons' kinetic energy due to electric field between the hemispheres. Electrons with energy of $E_{pass} \pm \Delta E$ are allowed to pass through the hemispheres and reach the MCP detector. Electrons with a kinetic energy higher or lower than this will collide with the outer or inner hemisphere, respectively, and be lost. The MCP detector multiplies the signal by production of a cascade of secondary electrons. These secondary electrons are accelerated towards a phosphorous screen and recorded by a CCD camera. The pass energy is kept constant during the measurement while the acceleration or retardation voltage in the electrostatic lens system is swept, which leads to the measurement of electrons with different kinetic energies. The resolution of the analyzer is given by the width of the detection channels of the detector in combination with the bandwidth of analyzer. The value of the analyzer resolution can be minimized by reducing E_{pass}, which leads to improved resolution but also a lower signal intensity.

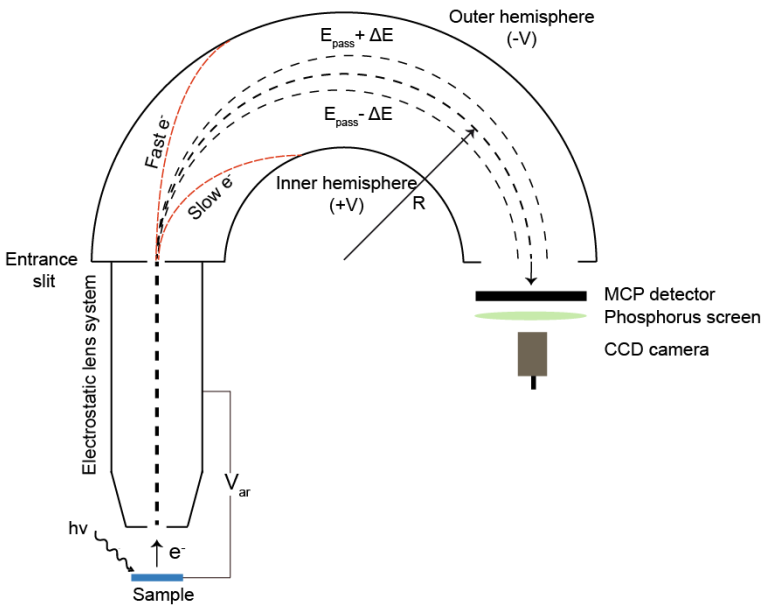

Figure 2.3. Schematic of a hemispherical electron energy analyzer.

Thus one needs to carefully choose a balance between the resolution and signal strength. The bandwidth of the analyzer depends on E_{pass} and of the size of the entrance slit. Assuming the entrance and exit slit to have the same size the bandwidth is given by the following formula [38]

$$\Delta E_A = \frac{E_{pass} S}{2R} + \frac{\alpha^2 E_{pass}}{4}, \qquad (2.6)$$

where S is the width of analyzer entrance slit, R is the mean hemispherical radius of analyzer and α is half of acceptance angle of emitted electrons. In the present case the assumption of equal entrance and exit slit sizes is incorrect since multichannel detection in combination with an open exit slit is employed. Nonetheless equation (2.6) gives a rough idea of the analyzer bandwidth and thus resolution.

2.1.3 Analysis of Photoemission Spectra

The XP spectrum consists of a main photoemission peak and some additional features which one needs to consider for the analysis of the data. Sources of broadening in the main line (no loss line) largely include natural line width, instrumental limitation and vibrational broadening. The finite lifetime of the core hole causes the natural line width which has a Lorentzian distribution and is governed by Heisenberg's uncertainty principle $\Delta E \times \Delta t \geq \hbar$. However, one typically cannot estimate the lifetime as normally the lorentz-broadened phonon peaks cannot be resolved in surface studies other than in rare cases [39]. The Lorentzian width is not significantly altered by the chemical environment of the atom as the lifetime of the excited state is approximately an energy level specific property [40]. The lifetime broadening contribution is mostly a few tenths of an eV for the low-Z atoms. The instrumental broadening (monochromator and analyzer resolution) is described by a Gaussian line profile. Vibrational broadening is often represented by a Gaussian distribution as well, since the vibrational components are usually not resolved. In the analysis the photoemission lines or components are often fitted with a convolution of a Gaussian and a Lorentzian distribution. Typically this is purely phenomenological and does not give a value for the lifetime of the excited state (as explained above).

The photoemission spectra of solid materials include a main line and additional features. The photoelectrons with no loss in energy gives rise to a main line whereas a large fraction of the photoemitted electrons lose energy by inelastic collisions (known as secondary electrons) when moving towards the surface, thus resulting in the background signal (inelastic tail). These secondary electrons are responsible for the background at the high binding energy side. Most often, the background signal consists of a featureless part and some broad features of specific energies. These additional features can be due to both intrinsic and extrinsic losses (see satellites discussion in section 2.1).The background

subtraction is a crucial step, as the estimation of the real shape of the background is hard to estimate. In the present work, Shirley and polynomial backgrounds have been used.

Auger lines and spin-orbit splitting also influence the appearance of the photoemission spectra. The Auger process starts with the creation of a core hole (with energy E^{core}). From there, the core hole is filled with an electron (of energy E^1) from a level at higher energy and the released energy is transferred to another electron (of energy E^2), which is finally ejected from the system as an Auger electron. The Auger electron kinetic energy is defined solely by the electron energy levels of the system and therefore is not dependent on the energy of the light that is used. **Spin-orbit splitting** arises due to the magnetic interaction between the spin $\vec{s}$ and the orbital angular momentum $\vec{l}$ of electrons in an unfilled subshell, which explains the fine structure of spectral lines. In photoemission spectroscopy, when a core hole is created in a subshell orbital with $\vec{l} > 0$, this leaves an unpaired electron in the final state. The magnetic interactions among the two spin states and the orbital angular momentum of the electron results in two energetically different states given by total angular momentum. Figure 2.4 presents an example of spin orbit splitting of a Ti 2p line measured on a rutile TiO_2(110) crystal. The final state in the photoemission for Ti 2p level gives either j = 1/2 or 3/2, resulting in two peaks separated by 5.7 eV.

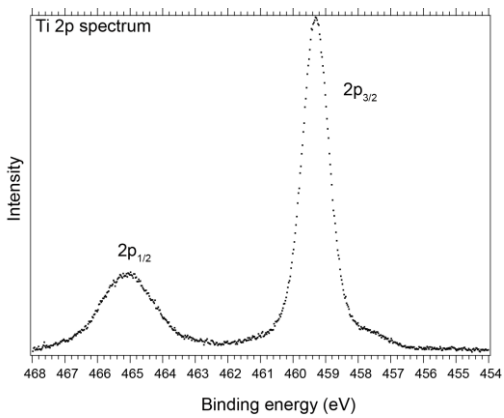

Figure 2.4. Spin-orbit splitting for the Ti 2p level measured on a rutile TiO_2(110) crystal. The value of the spin orbit splitting is 5.7 eV.

Chemical shifts (defined earlier in section 2.1.1) give very relevant information such as oxidation state and change in chemical environment etc. about the sample under investigation. The N 1s spectra in Figure 2.5 represents the three different chemical states of the N atom in its initial state for a sample where fluorine doped tin oxide is (FTO) treated with (3-aminopropyl)-triethoxysilane (APTES) followed by attachment of perfluorophenylazide (PFPA). The peak at very low binding energy is related to the partial decomposition of the azide (N--N+-N-) into amines whereas the peak in the middle confirms the presence of two negatively charged nitrogen ions N-, which are chemically

equivalent. The highest binding energy peak is attributed to a positively charged nitrogen ion. The binding energy of an ion increases with increase in the positive charge on it whereas an increase in negative charge leads to a decrease in binding energy and can be explained in terms of a screening effect[31].

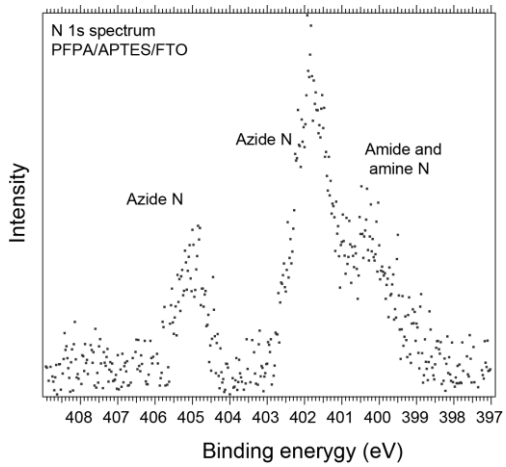

Figure 2.5. N 1s XPS spectra of FTO treated with APTES followed by attachment of PFPA.

2.2 Ambient Pressure X-ray Photoelectron Spectroscopy (APXPS)

Ultrahigh vacuum (UHV) studies can be the starting point to study the fundamental properties of surfaces interacting with gases or vapors in controlled fashion. Although often very useful [41], UHV measurements have the disadvantage that they vary from real pressures, e.g. in catalysis, by many orders of magnitude. This is called the pressure gap [42,43]. One needs to deal with this pressure gap and thus there is a need to develop surface characterization techniques which can work under elevated pressures. In order to perform XPS under ambient pressures, one must first consider the primary limiting factor, which is the short IMFP of photoelectrons in a gas. Combining the kinetic theory of gases with a consideration of a Maxwell-Boltzmann distribution gives the formulation for calculation of the IMFP (λ):

$$\lambda = \frac{k_B T}{\sqrt{2} \cdot P \cdot \sigma}. \qquad (2.7)$$

In equation (2.7) k_B is the Boltzmann constant, T is the temperature, P is the pressure and σ is the collision cross-section. The IMFP is inversely proportional to the pressure, so it decreases with an increase in pressure, thus causing a loss of electrons by inelastic

scattering. This demands a short traveling distance in a high gas pressure regime. One can achieve this constraint using several stages of pumping between a nozzle close to the sample and the analyzer which ensures that a pressure of 10^{-8} mbar at the detector is obtained and that the distance (between the sample and nozzle) is roughly equal to the IMFP [44], thus ensuring that electrons reach the analyzer.

The APXPS experiments of this thesis were performed at the TEMPO beamline at the synchrotron SOLEIL. The electrons enter the aperture of a diameter of 0.3 mm which separates the SPECS Phoibos 150-NAP hemispherical electron analyzer from high pressures in the main chamber by a differential pumping system. There are four distinct stages of differential pumping between the aperture and the detector (Figure 2.6).

The first pumping stage reduces the pressure by four orders of magnitude with respect to the main chamber pressure. The first pumping stage is equipped with an electrostatic lens, the prelens, which focuses the photoelectrons onto an aperture of diameter 2 mm. In addition, the prelens contains electrostatic deflectors to adjust the analyzer focus. The 2 mm aperture separates the prelens from the second pumping stage. The second and third pumping stages contain an electrostatic lens element in each stage which is separated by an iris aperture. The lens element in the second stage focuses the electrons onto the iris aperture. The smaller the size of this iris aperture the higher pressure difference is between the high pressure chamber and the pumping stages, although this sacrifices electron intensity. The second electrostatic lens in the third stage focuses the electrons transmitted through the iris onto the entrance slit. The fourth and last pumping stage includes the analyzer and detector which secure the pressure for the detector below a limit of 5×10^{-8} mbar [45].

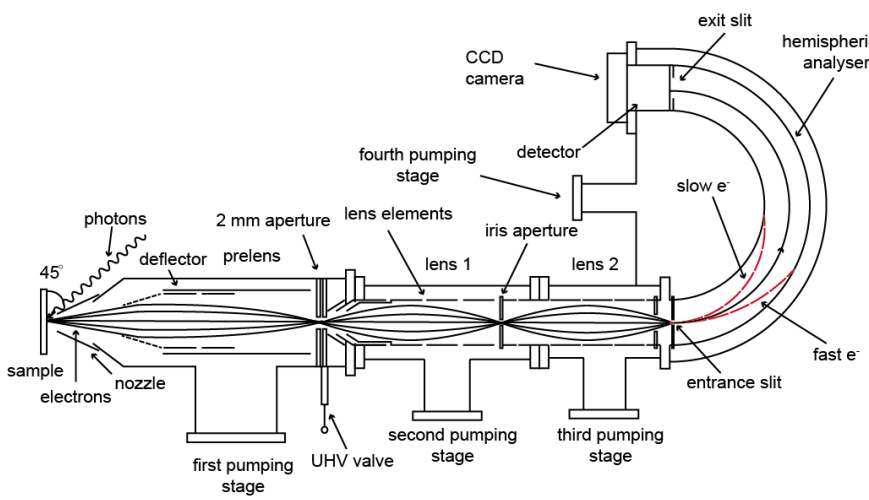

Figure 2.6. Schematic of hemispherical electron energy analyzer with representation of distinct pumping stages of APXPS, TEMPO beamline. Figure copied from Ref.[46] with permission of author.

2.3 Scanning Tunneling Microscopy

2.3.1 Principle and Theory

Scanning tunneling microscopy (STM) provides direct real-space images of surface structures with atomic resolution (in the sub-Å range). The STM was invented by Gerd Binnig and Heinrich Rohrer [47], who received the Nobel Prize in 1986 "for their design of the scanning tunneling microscope"[48].

The principle of STM is based on the quantum mechanical phenomenon of tunneling through a potential barrier. Ideally, an atomically sharp metal tip (usually made of tungsten or a platinum-iridium alloy) is brought into close proximity – some Å – of the sample, which needs to be sufficiently conducting. The latter condition implies that only conductors and semiconductors can be studied, while insulators are out of reach for STM. A bias voltage is applied between the tip and sample, which induces a net flow of electrons either from the tip to the sample or vice versa as determined by the polarity of the applied bias. A positive bias on the sample results in a flow of electrons from occupied states of the tip to unoccupied states of the sample, and the resulting STM image will show the unoccupied states. Figure 2.7 presents the schematic for the tip and the sample energy levels where a positive bias is applied. In the case of a negative sample bias the electron flow will be reversed and results in a STM map of the occupied states. The flow of electrons gives rise to a small, observable current, termed "tunneling current" (typically with a magnitude on the order of pA-nA [49]).

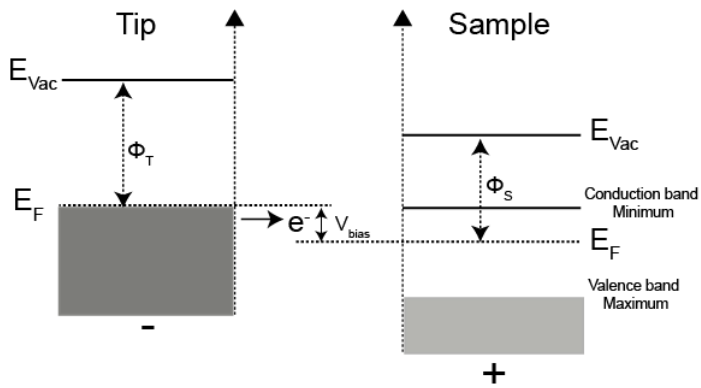

Figure 2.7. Schematic of the tip and the sample when a positive V_{bias} is applied to sample. Here, Φ_T, Φ_S are work functions of tip and sample.

The tunneling current (I) through a barrier can be approximately expressed by [50]

$$I \propto \exp\left[-\left(\frac{2d}{\hbar}\right)\sqrt{2m\Phi}\right], \quad (2.8)$$

where d is the distance between tip and sample, m the electron mass, and Φ the tunnel barrier height (essentially the work function of the sample surface). As can be seen from equation (2.8), the tunneling current is highly sensitive to changes in the tip-sample distance and changes roughly by an order of magnitude as a result of an Å variation in d, allowing atomically resolved STM images. The measurement of I gives the information of surface topography. Even if equation (2.8) gives the main idea for instrument, it is a very crude approximation. To obtain a quantitative description, the involvement of wave functions for the tip and sample is needed (with assumption of almost no interaction between tip and sample). A quantitative description of the tunneling current was developed by Tersoff and Hamann [51], who made use of Bardeen's [52] transfer Hamiltonian. According to Tersoff and Hamann the tunneling current can be written in a fashion similar to Fermi's Golden rule:

$$I = \frac{2\pi e}{\hbar}\sum_{t,s} f(E_t)\,[1 - f(E_s + eV)]\left|M_{t,s}\right|^2 \delta(E_t - E_s), \quad (2.9)$$

where *f(E)* is the Fermi function and the *t* and *s* subscripts stand for tip and surface, V is the applied voltage, $M_{t,s}$ is the tunneling matrix element between the states of the tip (Ψ_t) and surface (Ψ_s), and E_t and E_s are the energies of the tip and surface states. The delta function (δ) takes care of energy conservation by elastic tunneling.

To evaluate the tunneling current, it is crucial to calculate $M_{t,s}$, which can be written as (using Bardeen's approach)

$$M_{ts} = -\frac{\hbar^2}{2m}\int\left(\Psi_t^*\vec{\nabla}\,\Psi_s - \Psi_s\overrightarrow{\nabla\,\Psi_t^*}\right)\cdot d\vec{S}, \quad (2.10)$$

where the surface integral is over any surface situated entirely within the vacuum region separating the tip and sample surface. The calculation of matrix elements requires the knowledge of tip and surface wave functions. Generally, the exact atomic structure of the tip is unknown and assumptions have to be made. Tersoff and Hamann approximated the tip by a spherical potential with the center located at r_0 and, in addition, limited their theory to low temperature (room temperature or below) and voltages (~ 10 meV, for metallic surfaces) to calculate the tunneling current, which in turn depends on the local density-of-states (LDOS) of the sample surface at Fermi level written as following:

$$I \propto \sum_s |\Psi_s(r_0)|^2 \delta(E_s - E_F) \equiv \rho(r_0, E_F). \quad (2.11)$$

Here $\rho(r_0, E_F)$ is the surface LDOS at the tip Fermi level (E_F). Equation (2.11) implies that the tip probes the LDOS of the sample surface instead of the topography of the surface.

2.3.2 Instrumentation for STM

A variable temperature scanning tunneling microscope STM XA (Omicron Nano-Technology) at the Université Pierre et Marie Curie in Paris was used for the measurements presented in this thesis. The instrument consists of a preparation chamber equipped with a sputter gun and a low-energy electron diffraction setup and an analysis chamber for STM measurements. The STM instrument mainly includes an atomically (ideally) sharp tip, piezoelectric scanners to control vertical and lateral movement of the tip, a vibration isolation unit, an electronic control system and conducting/semiconducting sample (cf. Figure 2.8).

Homemade atomically sharp tips obtained from chemically etched tungsten wires and cleaned by Ar^+ sputtering and annealing were used for the STM measurements presented in this thesis. The tip is scanned over the sample surface using a piezoelectric (PZE) scanner. The PZE scanner made from PZE materials is the one of the crucial components which has tendency to expand and contract depending upon the applied electric field. The PZE scanner expands or contracts by ~ 1 Å/mV, allowing ultrahigh precision in positioning the tip relative to the surface [35]. The STM XA uses a tubular PZE scanner, offers high resonant frequencies due to its compact design, and has the advantage of reducing the sensitivity to external vibrations. The tubular PZE scanner mainly consists of a piezo tube, and electrode inside the tube (inner electrode) and an outer surface regarded as external electrodes divided into four quadrants [53]. The longitudinal movement (z-direction) is obtained by applying a voltage to the inner electrode with respect to the external ones, resulting in contraction and expansion of the tube length. The lateral movement in x- and y- direction is achieved by applying voltages of different polarity on opposite sides of the quadrants.

Vibration stability is one of the key parameters for the acquisition of images with atomic resolution, which requires damping of possible vibrations. The vibration damping is ensured by the whole STM stage (tip, sample and scanner) being suspended on springs.

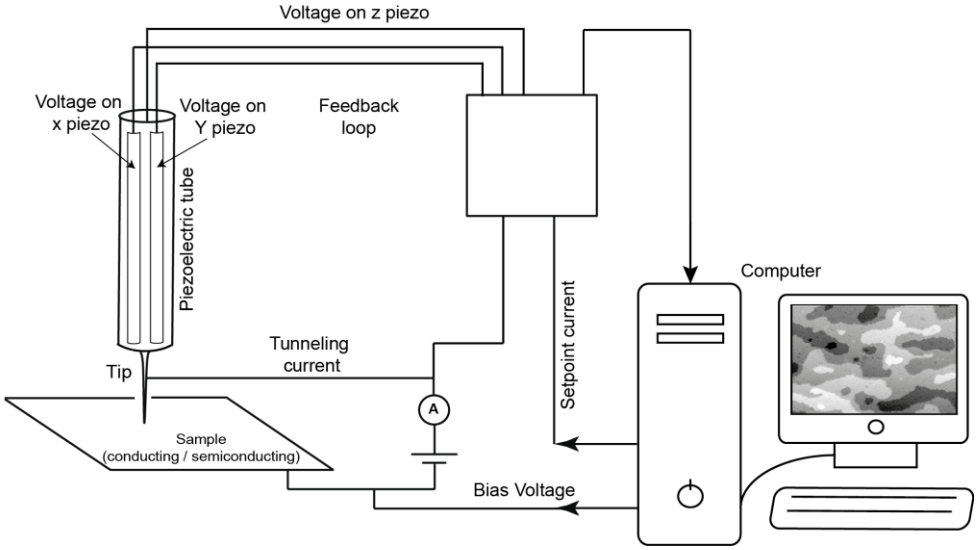

Figure 2.8. Schematic diagram of the STM setup. The sample is scanned by the tip using x and y piezos. A bias voltage, applied between tip and sample leads to a tunneling current. The tunneling current is maintained constant (CCM) with respect to a setpoint current value by controlling movements of z piezo using a feedback loop. The local height of topography is reflected by the voltage on the z piezo [54].

The scanning tunneling microscope operates in two different imaging modes: the constant current and constant height modes. The images presented in this thesis are acquired in constant current mode; in this mode, the tunneling current is kept constant while the tip-sample distance is adjusted by a feedback loop. The change in voltage applied to the piezoelement responsible for the adjustment of the tip-sample distance is recorded, and a plot of the piezo-feedback voltages versus the lateral tip positions gives the topographic image (for large-scale image) of the sample surface. However, in reality atomic-scale images are a complicated convolution of the topographic and electronic structure of the surface (discussed in equation (2.11).

2.4 Other Techniques

This thesis involves a few more standard characterization techniques which include fluorescence microscopy, water contact angle measurements, and scanning electron microscopy (SEM). I discuss them briefly below in view of their importance for the present work.

A Nikon Eclipse E400 epifluorescence microscope equipped with a CCD camera was used for fluorescence microscopy characterization (schematically shown in Figure 2.9). It is an

optical microscope, whose operation is based on the fluorescence and phosphorescence of materials. Light of a distinct wavelength is shone onto the sample. The light is absorbed by fluorophores, which re-emit at longer wavelength. Here, an amine-reactive derivative of a fluorescein dye named fluorescein isothiocyanate was used to label the samples to make them suitable for fluorescence microscopy. The dye has an excitation wavelength of 495 nm and emits at a wavelength of 525 nm [55].

The angle between a solid/liquid interface and the tangent of the liquid droplet is known as the contact angle. **Contact angle** measurements were performed to reveal the nature of the surface wettability and thus the hydrophobicity/hydrophilicity of the samples. Distilled water was used as a liquid for these measurements.

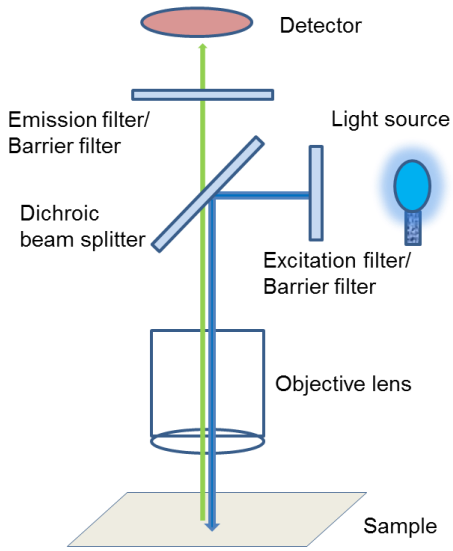

Figure 2.9. Schematic representation of the epifluorescence microscope.

In **Scanning electron microscopy (SEM)** a focused electron beam is used which is scanned over the surface of the sample to produce high quality images of the surface topography. The scanning electron microscopy offers high magnification with high resolution capabilities and a large depth of focus. This characteristic makes it a key tool for the analysis of a wide class of conducting, semi-conducting, and insulating materials. A strong beam of electrons, called the primary electron beam, is produced by thermionic emission. The primary beam of electrons interacts with the top atomic layers of the surface of the sample depending on the energy of the incoming electrons. This gives out a variety of signals that can be collected and processed to derive information about the morphology of the sample, atomic contrast in the sample, and the elemental composition of the top surface of the material. There are many different ways in which the primary beam may interact with the sample that emit either electrons or photons. Secondary electrons are

generated from only the top atomic layers of the sample and are used to analyze its topographic nature [56]. Primary electrons are backscattered in the interaction with the sample surface and produce images with a high degree of atomic number contrast. Finally, the primary beam of electrons can excite atoms of the sample that are stabilized by shell-to-shell transitions of electrons and cause either emission of X-rays or Auger electrons. Single microscopes mostly do not have the detectors for all of these signals. In the present case a secondary electron detector was used. Non-conducting samples need to be coated either with gold or platinum to avoid charging. In the present work the samples were coated with a thin film (< 20nm) of platinum.

Atomic force microscopy (AFM) is one of the versatile tools in the category of scanning probe microscopy techniques. It has high resolution, gives very high topographic contrast, and can evaluate direct height profiles of samples[57]. There is no need to coat the non-conducting samples for imaging, unlike in SEM. It can be used for imaging, force measurements, as well as manipulation of atoms at the nanoscale. In the atomic force microscopy a sharp probe (the tip) mounted on a cantilever is scanned over the sample. As soon as the tip is brought very close (~0.1 nm – 1 nm) to the surface of the sample, the interaction between the tip and the sample surface leads to deflections in the cantilever. These deflections are typically measured using position-sensitive photodiode detectors by recording the position of a laser beam reflected from the top of the cantilever. The output from the detectors creates a micrograph for sample surface topography. The mode of operation can be divided into three categories depending upon the distance between tip and sample surface: contact mode, tapping mode (also known as intermittent mode), and non-contact mode. Each of these modes has its own advantages and disadvantages. Tapping mode has been used for the present work which has the advantage of a nondestructive nature.

3. Materials and Methods

This chapter includes the description of materials – such as coupling agents, nanoparticles, and substrates – and methods used for the preparation of the various surfaces studied in this work.

3.1 Materials

3.1.1 Molecules

The present thesis involves work with five organosilane molecules, namely (3-aminopropyl)triethoxy silane (APTES), 3-glycidoxypropyl trimethoxysilane (GPTMS), (3-mercaptopropyl trimethoxysilane (MPTMS), *n*-propyltriethoxysilane (PTES), and tetraethyl orthosilicate (TEOS). APTES and GPTMS serve as coupling agents, whereas the adsorption geometries of APTES, MPTMS, and PTES on rutile TiO_2(110) were investigated in detail with the background that PTES and MPTMS have been used as coupling agents in various applications [58,59].

A coupling agent is a material which is capable of forming a chemical linkage at the interface of two dissimilar surfaces and is frequently used to link organic-inorganic interfaces. **Organosilane** molecules consist of bi-functional groups with silicon at the center and have a generic chemical formula $R_nSi\ X_{(4-n)}$.The organic functional group (R-epoxy, amino, mercapto etc.) is generally a hydrolytically stable bond that can bind with organic materials, whereas the X functional group (methoxy ethoxy, etc.) hydrolyzes easily and can form a bond between inorganic materials and Si by liberating methanol or ethanol as side product [60]. APTES, with an amino group on an alkyl chain, is a popular agent to immobilize biomolecules such as proteins [61,62], enzymes, antibodies [63], and DNA useful for biomedical devices [64]. The purpose of APTES was to use its terminal amino group to bind with a **photocoupling agent**, perfluorophenylazide N-hydroxysuccinimide (PFPA-NHS), through the carboxylic end by liberating the NHS which creates a PFPA termination on the glass slide. The azide of the PFPA can be activated by light, heat, or electrons into a more reactive nitrene group, which can form stable covalent bonds by CH or NH insertion present in organic materials [65]. Immobilization of amine coated MIP nanoparticles on gold surface was achieved using carbodiimide coupling which include 11-mercaptoundecanoic (MUA) acid as coupling agent between a surface and MIP core-shell nanoparticles. TEOS and tetrakis(dimethylamino)titanium (TDMAT) are used as precursors for the growth of silicon oxide and titanium dioxide, respectively. Figure 3.1 depicts the structures of the organosilanes, MUA, and TDMAT molecules.

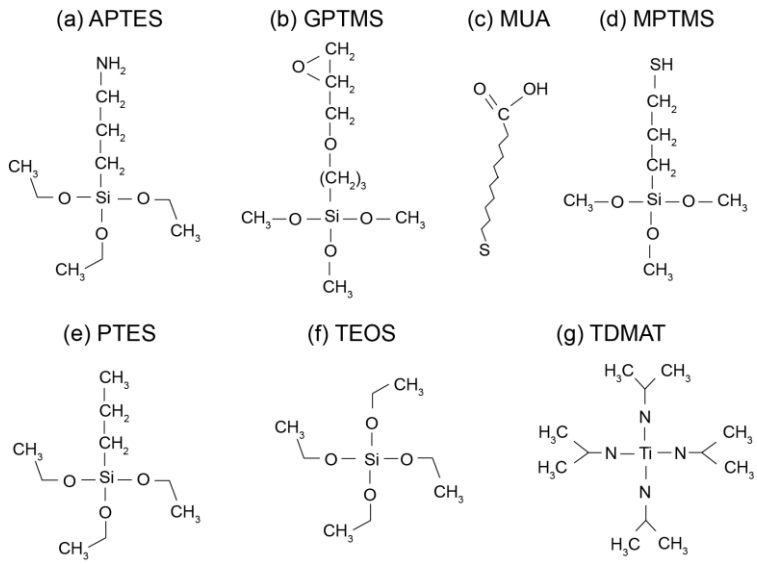

Figure 3.1. Chemical structures of (a) APTES, (b) GPTMS, (c) MUA, (d) MPTMS, (e) PTES (f) TEOS, and (g) TDMAT molecules.

3.1.2 Nanoparticles

MIP nanoparticles were used as model nano-objects for demonstrating the potential of the short coupling agent to form a covalent assembly. MIPs are synthetic receptors having selective molecular recognition ability towards a particular template (described in section 1.1). MIP nanoparticles were prepared using precipitation polymerization following a procedure described by Yoshimatsu *et al* . [66] with propranolol as the template molecule. Propranolol is a non-selective beta blocker used for the treatment of anxiety and hypertension. The non-imprinted polymer nanoparticles were also prepared using the same recipe as for the MIP particles, except that the template was absent.

Amine-functionalized core-shell MIP nanoparticles were synthesized by following the procedure reported by Hajizadeh *et al.* [67] The core consists of a MIP, whereas the shell is made up of amine groups which can react with the epoxide ring of GPTMS used in **paper 2** for covalent immobilization.

The gold-loaded reverse micelle nanoparticles (Au-RMNPs) were synthesized according to a literature procedure [68] using poly(styrene)$_{312}$-*block*-poly(2-vinylpyridine)$_{74}$ (32500-*b*-7800 gmol^{-1}), obtained from Polymer Source, as the amphiphilic diblock copolymer and a gold to pyridine loading of 0.5. For electrospray a solution with concentration 0.1 mgL^{-1} of Au-RMNPs in toluene:methanol (3:1 V/V) was used, and a small amount of methanol acts as polar solvent which is needed to causes a solvent cone in electrospray deposition.

3.1.3 Substrates

Microscopic glass slides, silicon oxide, and gold coated silicon oxide were used as model supports for the immobilization of MIP nanoparticles. Additionally, fluorine-doped tinoxide (FTO) substrates were used for XPS measurements to avoid potential charging on non-conducting samples. The FTO substrate is a glass substrate with a coating of electrically conductive fluorine-doped tin oxide.

The TiO_2(110) surface – the oxide surface of choice in **paper 4, 5, 6, and 7** – is one of the most well-studied oxide surfaces. Titanium dioxide has a wide range of applications due to its durability, biocompatibility, and environment adaptability [69]. TiO_2 is a wide band gap semiconductor with a band gap of ~3 eV and occurs naturally in three crystal structures: rutile, anatase, and brookite. Rutile TiO_2(110) is the most studied surface among all the TiO_2 surfaces as it is more stable compared to other low index surfaces [69,70]. The rutile TiO_2(110) surface contains of rows of sixfold-coordinated Ti atoms along the [001] direction that alternate with rows of fivefold-coordinated Ti atoms. The rows of the fivefold-coordinated Ti atoms are separated from the rows of the sixfold-coordinated Ti atoms by rows of three-fold coordinated oxygen atoms (cf. Fig. 3.2). The sixfold-coordinated Ti atoms are capped by twofold-coordinated oxygen atoms arranged in bridging positions (the bridging oxygen atoms). The excess charge from dangling bonds is fully compensated by the opposite charges of Ti and O atoms with no dipole moment in the [110] direction [69], and therefore the surface is charge neutral.

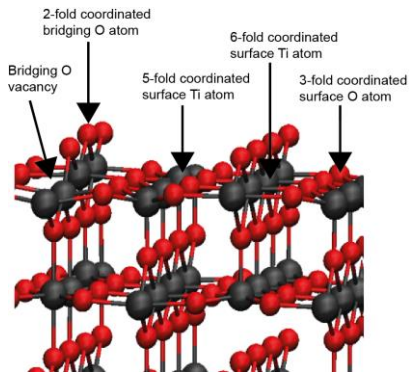

Figure 3.2 Ball and stick model for the rutile TiO_2(110) surface. Red and dark grey spheres represents O and Ti atoms, respectively.

The valence band is mainly comprised of O 2p states, whereas the conduction band is comprised of Ti 3d orbitals [71]. Surface and bulk defects arise due to the reduction of the TiO_2 crystal from Ar^+ sputtering and subsequent annealing in the surface preparation process. Bulk defects make TiO_2 an n-type semiconductor with donor levels in the band gap [69], which make the surface suitable for techniques like XPS and scanning tunneling

microscopy where the surface needs to be conductive. The surface defects are mainly due to bridging oxygen vacancies and subsurface defects that include titanium interstitials, which offer active sites to different species for adsorption and dissociation. A defect-induced band gap state exist at ~0.8 eV on the binding energy scale. These defect states normally originate from a decrease in positive charge on the Ti atoms [71] and can be associated with either subsurface Ti interstitials [72,73,74] or bridging oxygen vacancies [75,76,77].

The RuO_2(110) surface- The ruthenium dioxide is a metallic conducting oxide with rutile crystal structure (similar to TiO_2). The RuO_2 has potential application in heterogeneous catalysis and electronic industry [78].The RuO_2(110) surface used in **Paper 8** was prepared by heating the Ru(0001) crystal in the presence of O_2 pressure (5×10^{-2} mbar) [79].

3.2 Methods

Paper 1, 2, and **3** involve standard solution-phase based chemical methods to prepare the various surfaces of interest, whereas chemical vapor deposition (CVD) was studied in **paper 4, 5, and 7**. **CVD** is used to surface-deposit thin films with quite good homogeneity, where the vapor phase precursors form the desired deposit by chemical reaction in the vicinity or directly on the substrate surface. CVD can be initiated in three separate ways and is therefore categorized as follows: thermal CVD, plasma assisted CVD, and photo-initiated CVD [80]. It can be further categorized on the basis of working pressures as ultra-high vacuum CVD, low pressure CVD, and ambient pressure CVD. The present work used (near-) ambient pressure (~ 2 mbar) CVD, where the temperature of the substrate was increased gradually from room temperature to 800 K to monitor the real-time growth of silicon oxide. **ALD** is also a thin film deposition method which is very much similar in chemistry to CVD except that the reaction is divided into two halves to form layer by layer deposition [81]. ALD ensures extremely uniform, thin films with controlled thickness. The ALD method was used for the growth of TiO_2 on RuO_2 (**Paper 8**). The CVD and ALD were performed at the APXPS end station at the TEMPO beamline of the French synchrotron radiation facility SOLEIL.

Electrospray deposition uses high voltages to generate sprinkle of charged droplets from solution of the desired analyte, which forms fine droplets due to evaporation of solvent and breaks into smaller size by coulomb explosion [82] and get deposited onto the exposed substrate. It is a very useful technique for the deposition of non-volatile molecules in UHV. There is plenty of literature on the working principle of electrospray and on the setup we used for work [83] done in **paper 6**, where gold-loaded block copolymer reverse micelles were deposited on a TiO_2 surface in UHV.

4. Results

This chapter presents a brief summary of the papers included in this thesis.

4.1 Immobilization of MIP Nanoparticles on SiO_2 and Gold

To integrate the functional nano-objects with model supports, a short-linkage assembly of coupling agents was designed and studied after each step of the immobilization procedure (**paper 1).** Figure 3.2 gives an overall schematic for the process followed in **paper 1**.

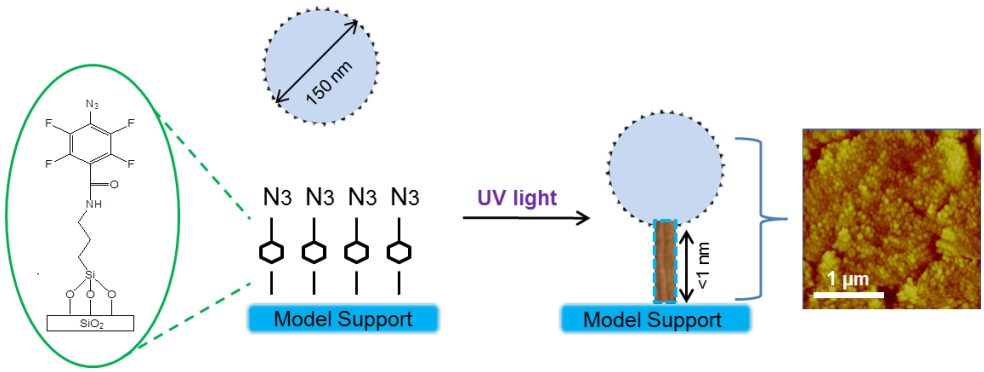

Figure 3.2. Schematic of the process used for the immobilization of MIP nanoparticles. Adapted from **Paper 1.**

In order to maximize the nanoparticle loading, the first goal was to achieve a high density of terminal amines on the glass surface while avoiding the aggregation of silane, which forms at increased concentrations of APTES [84]. Figures 1 and 2 in **Paper 1** show the contact angle measurements and fluorescence microscopy images for different concentrations of APTES. They show an increased hydrophobicity and fluorescence with increase in concentration. The optimal APTES concentration was 6% as it gives high fluorescence by reacting with the available amino groups and shows a relatively even distribution with minimum aggregation.

XPS measurements were performed at each step of immobilization. Analysis of the N 1s and C 1s lines (Figure 3.3 (a) and (d)) confirms the attachment of APTES [85]. Contact angle measurements confirm the successful PFPA modification. The water contact angle increased from 60º to 80º upon PFPA modification, reflecting the more hydrophobic nature of the PFPA compared to the APTES. All observed features (Figure 3.3 (b) and (e))

correspond to the expected elemental species for PFPA. For the MIP nanoparticle-modified surface a decrease of the water contact angle to 60º is observed due to the presence of polar COOH groups on the surface of the nanoparticles. Additional confirmation of attachment was verified by measurement of the C 1s and N 1s lines (Figure 3.3 (c) and (f)) and O 1s XP spectra (Figure 5 in **Paper 1**), where the presence of COOH groups was confirmed both in the O 1s and C 1s spectra. SEM images show very few particles on the reference sample (non-functionalized FTO) as seen from Figure 6 (a) in **Paper 1,** but there is a high density of immobilized particles once the FTO is functionalized with PFPA (Figure 6 (b) in **Paper 1**.

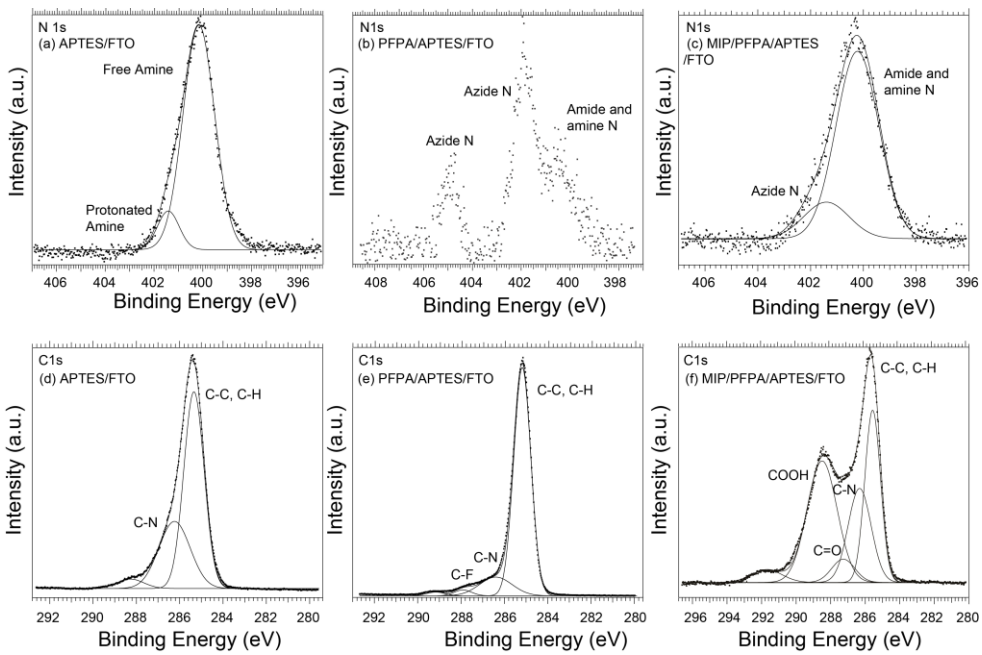

Figure 3.3. XPS characterization of the samples, which shows that the different steps of preparation steps depicted in Scheme 1 (**Paper 1**) have been successful. N1s XP spectra of (a) FTO treated with APTES, (b) FTO treated with APTES followed by attachment of PFPA. (c) FTO treated with APTES followed by attachment of PFPA and immobilization of MIP nanoparticles. C1s XP spectra of (d) FTO treated with APTES, (e) FTO treated with APTES followed by attachment of PFPA. (f) FTO treated with APTES followed by attachment of PFPA and immobilization of MIP. The Figure is adapted from **Paper 1**.

The linkage assembly for the MIP nanoparticles is proven to be nondestructive as shown by radioligand binding analysis, where the MIP immobilized surface binds 26.6 fmol of tritium-labeled propranolol compared to no binding in a non-imprinted polymer (NIP) immobilized on the same kind of surface. To initially test the masking capability of the present method, the PFPA-modified surfaces loaded with MIP nanoparticles were covered with a photomask before exposure to UV light. The SEM image in Figure 3.4 indicates

that the pattern is consistent with the dimensions of the photomask, thus enabling successful nanoparticle pattern creation using this method.

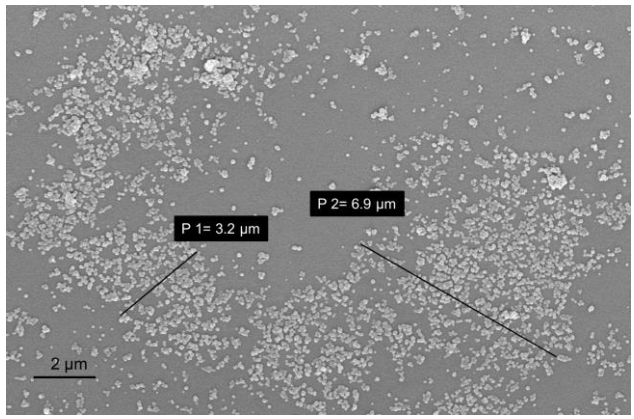

Figure 3.4. SEM image of the MIP immobilized on PFPA functionalized surface which shows the patterns consistent with that of the photomask used at the time of UV light exposure.

The other approach (**paper 2**) for the covalent immobilization of amine-functionalized MIP core-shell nanoparticles involves the GPTMS as the coupling agent, where the epoxide ring makes a covalent link with the amine group through an epoxide ring opening reaction [86] This approach results in the uniform distribution of MIP core-shell nanoparticles, while, simultaneously, maintaining their functionality. The scheme for the immobilization process is presented in Figure 3.5.

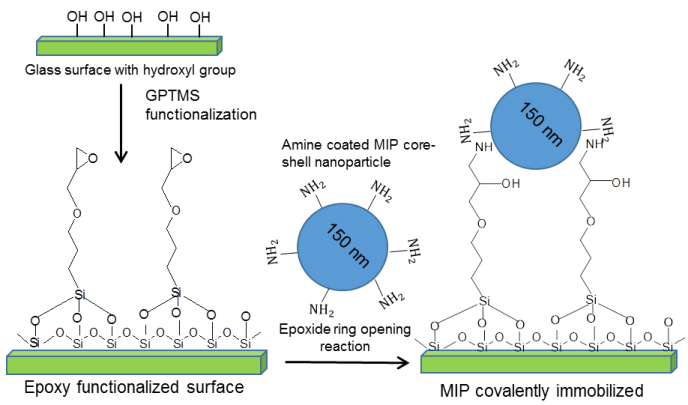

Figure 3.5. Scheme for the immobilization of MIP core-shell nanoparticles on glass surface. Figure rearranged from **Paper 2.**

The contact angle (Figure S1 in **Paper 2**) for the GPTMS functionalized surface exhibits an angle of 55º [87] compared to that of a blank slide with < 5º, which can be traced back

to the fact that GPTMS is more hydrophobic than the blank surface due to the presence of epoxide groups. The peaks in the C 1s XP spectra correspond to hydrocarbon and epoxide for the GPTMS functionalized glass surface, which further verifies the attachment of GPTMS (Figure 3.6). The increase in epoxide peak intensity at grazing emission indicates (Figure 3.6) that the epoxide groups point away from the surface, which is desirable for subsequent immobilization of the amine-functionalized MIP core-shell nanoparticles.

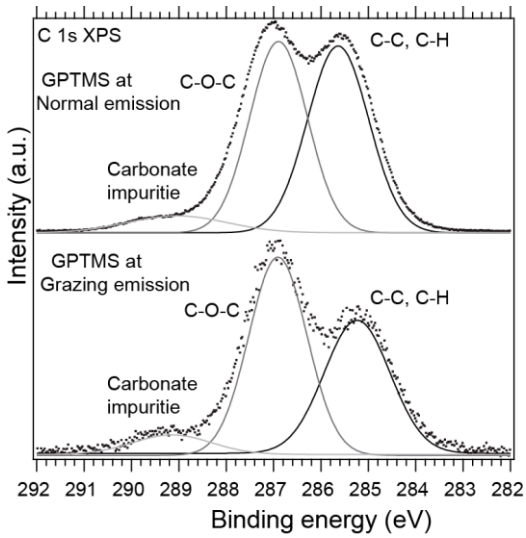

Figure 3.6. Comparison of C 1s spectra of Si-Epoxy measured in normal emission (NE, more bulk sensitive) and grazing emission (GE, more surface sensitive) geometries. The Figure is adapted from **Paper 2.**

The MIP core-shell nanoparticle immobilization on the surface results in a decrease of the contact angle compared to the GPTMS functionalized surface, reflecting the hydrophilic nature of the amine-functionalized MIP surface. The confirmation of immobilization of the amine-functionalized MIP particles is also supported by the AFM topographic and fluorescence microscopy images (Figure 1 (c) and 3(c) in **Paper 2**). The C 1s, N 1s, and O 1s XP spectra for the MIP core-shell nanoparticles immobilized on the GPTMS surface collectively affirm every feature expected from the structure of the MIP core-shell nanoparticles. To confirm the availability of binding sites after the immobilization process, the MIP-treated surfaces were characterized by radioligand binding studies using radioactivity sensitive photographic films. When brought in close contact with the radioisotope (^{3}H) the film blackens to produce the image. The autoradiography image for MIP immobilized on GPTMS functionalized surface shows a large contrast (compared to the blank Figure 5 (A) in **Paper 2**), confirming the presence of the template (labeled with ^{3}H) and produces large radioactive emission. The nonselective binding of template for the NIP particles immobilized (Figure 5 (C) of **Paper 2**) on a GPTMS-functionalized surface

also shows some contrast. To verify the selectivity of the template molecules, the competitive compounds (analogous in structure to propranolol) unlabeled free base propranolol, pindolol, and 1-amino-3-(napthalen-1-yloxy) propan-2-ol (ANOP) were tested together with the labeled propranolol. Figure 5 (E) in **Paper 2** indicates that the binding of labeled propranolol decreased in the presence of the unlabeled propranolol due to complete similarity in structure, whereas the presence of the other two analogues did not affect the binding significantly (Figure 5 (F) and (G) in **Paper 2**).

In **Paper 3,** the methodology for immobilization of amine functionalized MIP-core shell nanoparticles on Au surface was explored and characterized at each step. The carboxylic groups resulting from MUA based SMAs were activated using N-hydroxysuccinimide (NHS) and 1-ethyl-3-(dimethylaminopropyl)carbodiimide hydrochloride (EDC) molecules. The activated carboxylic groups then bind covalently with amine functionalized core-shell nanoparticles. The reaction steps are summarized in Figure 3.7. The successful functionalization of Au surfaces with SAMs, activation step, and immobilization of MIP particles was confirmed with spectroscopic and microscopic techniques in detail.

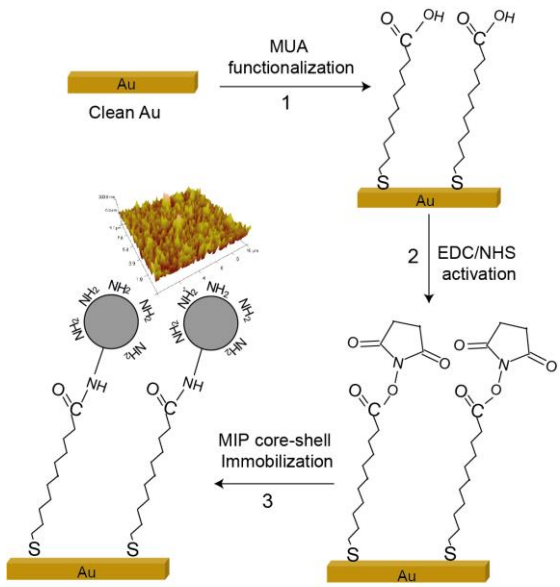

Figure 3.7 Scheme for the immobilization of MIP core-shell nanoparticles on gold surface. Figure rearranged from **Paper 3**.

4.2 Adsorption of Silane Molecules on the Rutile TiO_2(110) Surface

The adsorption of three silane molecules on a rutile TiO_2(110) surface, APTES, PTES, and MPTMS, was investigated. All the three molecules were found to bind dissociatively to the surface. In case of APTES (paper 4), this finding is in contrast with the results of Gamble *et al.* [88], according to who APTES molecularly desorbs at 220-500 K. In the present work (**Paper 4**), the appearance of the C 1s, N 1s lines and broadening of the Si 2p line (Figure 2 and in **Paper 4**) confirm the presence of APTES even at room temperature, and STM images further suggest the dissociation of APTES molecules. Both the dissociated ethoxy groups and residue of APTES bind to the surface, as can be seen in Figure 3.8 in **Paper 4**.

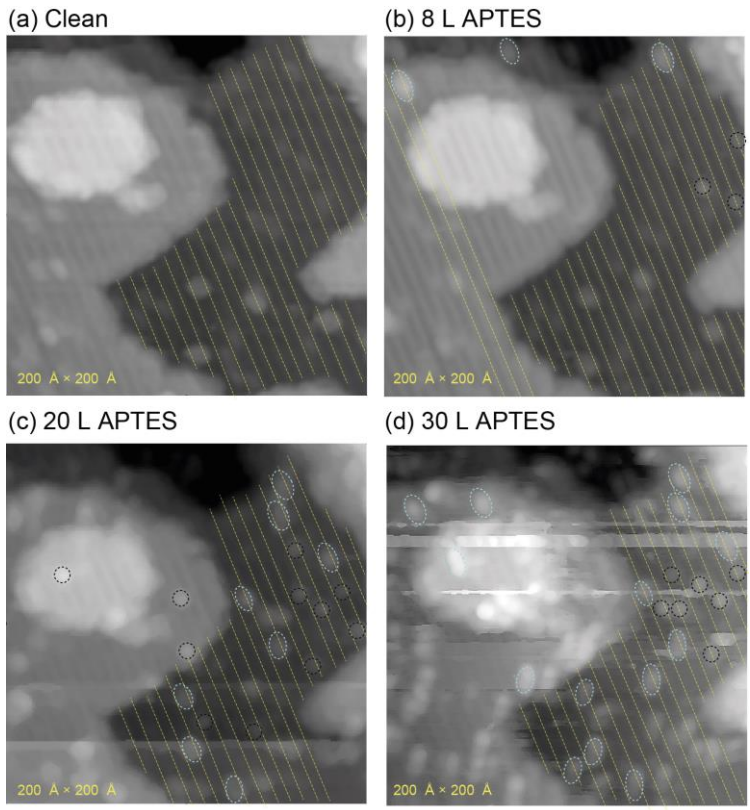

Figure 3.9. STM images (200Å × 200Å) of (a) clean, (b) 8 L, (c) 20 L, and (d) 30 L APTES dosed reduced TiO_2(110) at room temperature, where circle and ellipse represents the dissociated ethoxy groups and residue of APTES molecules respectively. V_{bias}= 2.0 V, I= 50 pA for (a)-(c) and V_{bias}= 2.0 V, I= 30 pA for (d). Dashed lines represent Ti rows. Adapted from **Paper 4**.

In **Paper 5** angle-dependent XPS measurements suggest that the PTES binds with an alkyl chain pointing towards the surface for half monolayer coverages, whereas the apparent reverse behavior is observed for a monolayer (Figure 3.9(a) and (b)). In the case of MPTMS, the thiol group points away from the surface for a half monolayer coverage as reflected from the C 1s lineshape at two different emission angles (Figure 3.9(c)). The sticking coefficient was found to be larger for PTES compared to MPTMS.

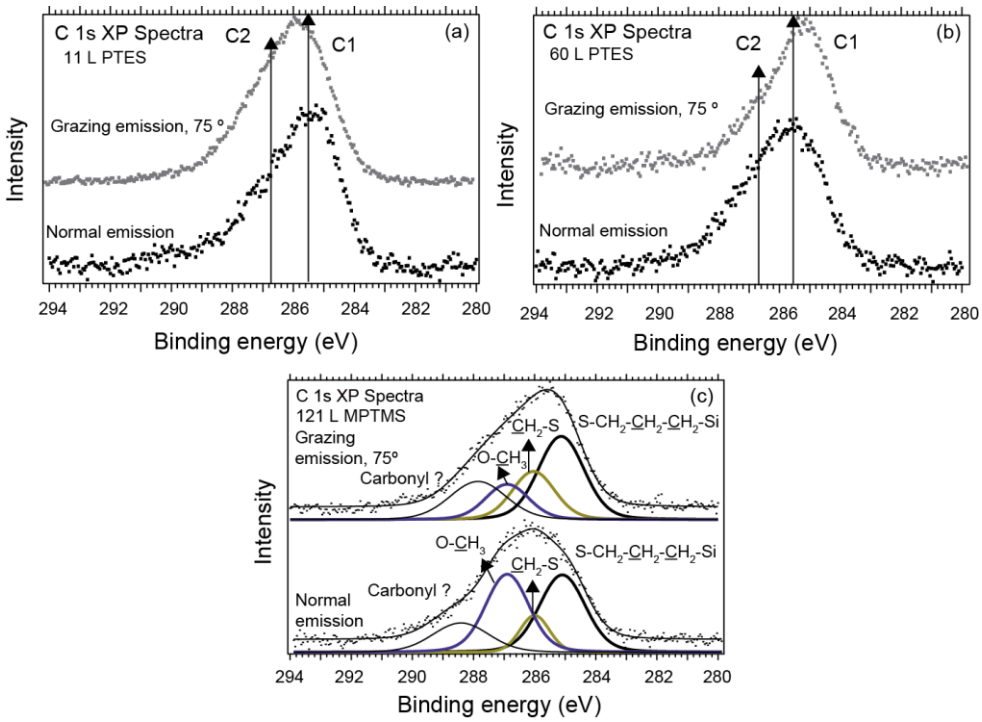

Figure 3.9. C 1s XP spectra for PTES/TiO_2(110) (a) for 11 L and (b) for 60 L of dose. (c) C 1s spectra for 121 L of MPTMS/ TiO_2(110). Adapted from **Paper 5**.

4.3 Gold-loaded Block Copolymer Reverse Micelles on the Rutile TiO_2(110) Surface

In **Paper 6** the electrospray deposition method was used for deposition of gold-loaded reverse micelle nanoparticles (Au-RMNPs) on a rutile TiO_2(110) surface under vacuum. Atomic oxygen and an oxygen plasma were tested to remove the polymer shells from the Au nanoparticles to result a in Au-decorated TiO_2 surface useful for various applications. XPS was used to follow the deposition of nanoparticles and removal of the polymer shell. The Au 4f, C 1s, and N 1s XP spectra (Figure 3.10) confirm the deposition of the Au-

RMNPs. Atomic oxygen proved to be slightly more efficient in the removal of the polymer shell in comparison to the otherwise widely used oxygen plasma. The set of experiments shows the potential of the electrospray deposition method to prepare surface-supported nanoparticles in vacuum for further fundamental studies.

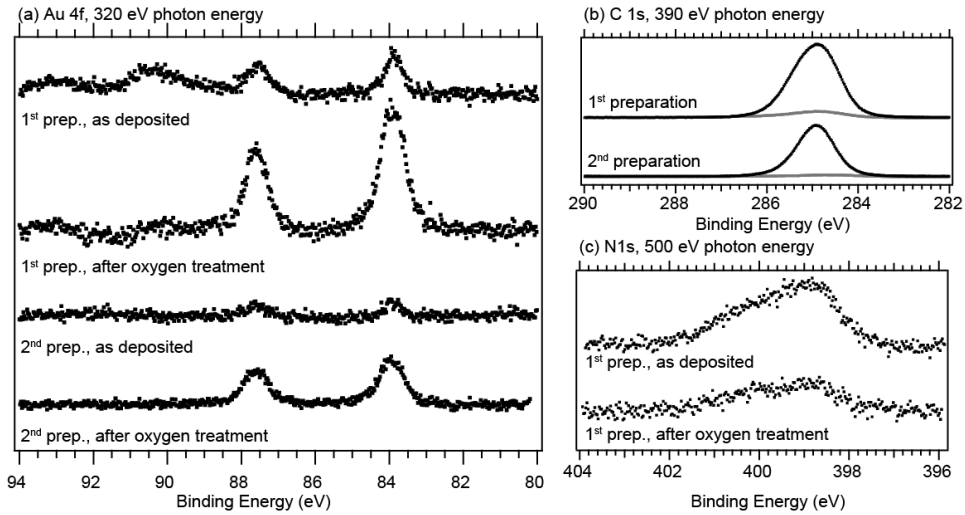

Figure 3.10. XP spectra of Au-RMNPs on TiO2(110). (a) Au 4f spectra before and after the oxygen treatment of the first and second preparations. (b) C 1s spectra of both preparations before (black) and after (grey) the polymer shell removal. (c) N 1s spectra of the first preparation before and after removal of the polymer shell. Figure rearranged from **Paper 6**.

4.4 Growth of Silicon Oxide on the Rutile TiO_2(110) Surface

In **Paper 7** TEOS, an organosilane, was used for the CVD growth of silicon oxide on a rutile TiO_2(110) surface. The growth was monitored by APXPS. It is observed that the TEOS molecules at room temperature adsorb dissociatively [89] with respect to the ethoxy chains. An additional surface reaction of the dissociated ethoxy groups leads to formation of carboxylic species, probably acetic acid (cf. the C 1s and O 1s spectra in Figures 3 and 4 in **Paper 7**). The exposure of the sample to the vapor pressure of TEOS results in a thick multilayer on top of the TiO_2 crystal: the Ti 2p line could not be observed anymore. Further, in a temperature series, in which the sample was annealed to ~800 K in the presence of TEOS (pressure of 2.3×10^{-4} mbar), SiO_2 was generated, monitored by C 1s and Si 2p XPS (Figures 7(a) and (b) in **Paper 7**). Additional growth of SiO_2 in a second temperature run in the presence of TEOS at a pressure of 2.3×10^{-7} mbar is shown in Figure 3.11.

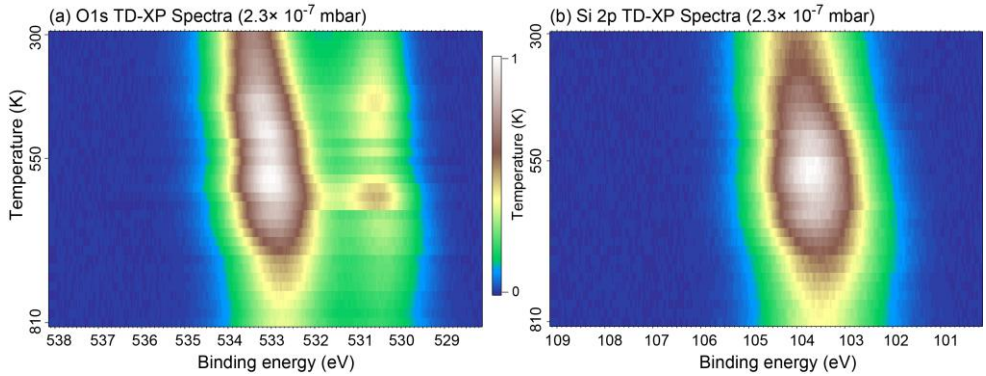

Figure 3.11. O 1s (a) and (b) Si 2p TDXP spectra for TEOS adsorbed on the silicon oxide layer grown on the TiO_2 (110) surface in the first TDXPS experiment. The color scale represents the intensity of peaks. Adapted from **Paper 7**.

In the O 1s spectra an intermediate species is observed between SiO_2 and the support, which is assigned to a of mixed titanium/silicon oxide [90,91]. The SEM images (Figure 3.12) give a clear indication for the change in surface morphology after the growth of SiO_2.

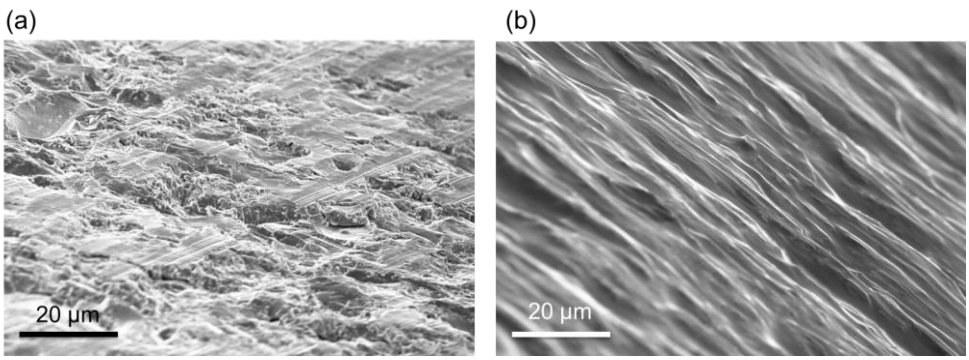

Figure 3.12. SEM images of the edge of (a) a clean TiO_2(110) crystal and (b) the silicon dioxide layer formed on a TiO_2(110) single crystal surface in the second temperature run.

4.5 Growth of TiO_2 on the RuO_2(110) surface

The ALD growth of TiO_2 on RuO_2(110) was investigated in **Paper 8** using APXPS. TDMAT was used as molecular precursor in combination with water and ALD was performed at 110 °C. During the First ALD cycle, the presence low binding energy shoulder in Ti spectra (Fig. 2 (a)) and dimethyl amine and imine species in N 1s spectra (Fig. 3 (a)), in addition to amido species bonded to Ti atom confirms the side reactions of

TDMAT. The second half cycle with water shows a pressure dependence to remove the amido ligand and formation of the alkylammonium cations. The relative amount of nitrogen species for three full ALD cycles is summarized in Figure 3.13. It is clear, that with increase in ALD cycles, fewer byproducts were formed. The resulting interface between TiO_2 and RuO_2 was found to be distinct, without any intermixing of two materials.

In other experiment, to investigate the effect of temperature on surface species, the TDMAT was dosed clean RuO_2 at room temperature, which leads to the formation of multilayer (Figure 8 and 9 in **Paper 8**). The multilayer desorbs at 40°C and imine species, which was absent at room temperature start to appear after 60 °C and became significant at 110°C. This indicated that heat is required to form the imine species.

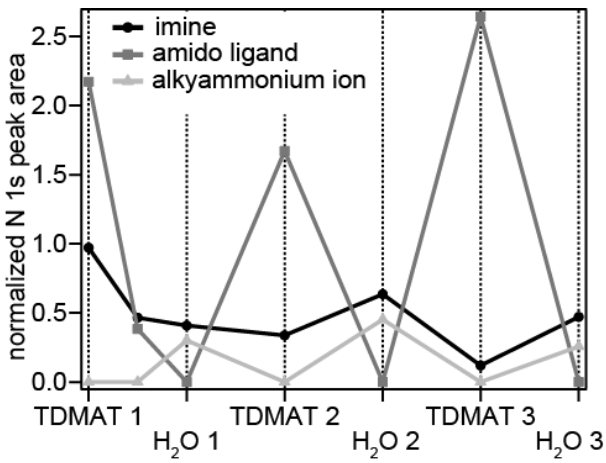

Figure 3.13. The change in the N 1s peak components throughout the ALD half-cycles. The peak areas are normalized to the amine component. The first TDMAT half-cycle was after exposure to 0.1 mbar, the second and third TDMAT half-cycles are at pressures of 0.02 mbar. The first two H_2O cycles are at 0.1 mbar, the third is at 0.01 mbar. The data point between the first two half-cycles corresponds to a water pressure of 1 x 10^{-5} mbar. All the ALD cycles were conducted with RuO_2 temperature of 110 °C. Adapted from **Paper 8**.

5. Summary and Future Outlook

The research work presented in the thesis started with the integration of pre-made functional MIP nanoparticles with model surfaces, an initial step towards working nanosensors (paper 1-3). Firstly, the covalent assembly of short coupling agents has been studied, and it has been demonstrated that nano-objects based on organic materials can be immobilized without affecting their functionality. The developed photoconjugation method may also be used to combine unmodified MIPs with other functional materials to prepare new composites for other applications including affinity separation and catalysis. The MIP core-shell nanoparticles immobilized using the epoxide ring opening reaction also preserve their molecular selectively for propranolol and its structural analogues in an aqueous medium. The carbodiimide based coupling chemistry has been used to immobilize the MIP core-shell nanoparticles on a Au surface, which is one of the ideal surfaces for transducers in optical and electrochemical sensing applications. The most important advantage of these methods is that MIP nanoparticles can be immobilized directly on the transducer surfaces, which provides a generic approach to the application of organic MIPs for sensor applications. Given the easy operation in photochemical based immobilization methods and the possibility to create nanoparticle patterns using a suitable photomask, the photochemical immobilization method should be useful for development of different types of MIP-based chemical sensors.

Although silane-based immobilization methods result in the desired surfaces for sensor applications, the aggregation of silane molecules was observed up to some extent. Previously, the silane coupling agents had not been studied extensively in a detailed and controlled fashion in order to understand the adsorption with respect to their available functional groups (R or X), i.e. which terminal group is pointing away from surface (R or X) for further coupling with other functional materials and by which terminal groups silane attach to oxide surfaces. In **Papers** 4 and 5, CVD-deposited silane layers of APTES, PTES, and MPTMS have been studied which gives insight into adsorption geometries of silane molecules on the rutile TiO_2(110) surface. Specifically, in the case of APTES at lower coverage, the amine functional group, which is responsible for further immobilization, points towards the surface. This finding is in contrast to other literature claiming that the amino group points away from the surface. However, a mix of amine groups pointing away and towards the surface has been observed at the high pressure measurements which forms multilayers.

The fundamental understanding of adsorption of silane molecules on surfaces will open the door to further studies of immobilization of nano-objects (biomolecules, dyes and functional structures). Recently, silane-modified (3-mercaptopropyl)trimethoxysilane) TiO_2 nanoparticles have been shown to double the conversion efficiency in DSSCs by

increasing the loading of ruthenium based N3 dye due to the increase in the surface area of the nanoparticles [92]. The study of the ruthenium-based N3 dye on silane modified TiO_2 can also establish useful insights regarding the interface. The SAM of silane grown in a controlled fashion can be tested and used in biomedical and semiconductor devices to compare with conventional methods. Silane-based coatings also serve as a protective layer against corrosion of metals, so systematic and controlled UHV measurements of silane molecules on metal surfaces can provide in-depth knowledge of metal-organic interfaces. Clean studies concerned with the effect of various species such as oxygen, nitrogen, carbon dioxide, and water vapor can shed some light on the protection mechanism of silane-based protective layers. The study of copper films over silane terminated layers (such as 3-(triethoxysilyl)propionitrile) is also an interesting problem as SAMs are proven to form good diffusion barriers with sizes of < 2nm, which is needed in ultralarge integrated circuits.

An interesting approach to obtaining the high catalytically active surface for CO oxidation was to integrate the Au nanoparticles with physical barriers to avoid sintering on TiO_2 surfaces. As an initial step Au-RMNPs were deposited in vacuum for the first time using the electrospray, and atomic oxygen proved to be an efficient method to remove the polymer shell.

The real-time monitoring of CVD growth of SiO_2 on TiO_2 throws light on the molecular processes during SiO_2 formation. The presence of the TEOS vapor changes the surface processes significantly and alter the equilibrium of the surface reaction towards the formation of acetic acid and away from the simple binding of ethoxy groups at room temperature. The presence of an intermediate oxygen species during the CVD process at a temperature of around 600 K was attributed to a mixed titanium/silicon oxide.

The investigations of ALD growth of TiO_2 on RuO_2 revealed that the side reactions were present prominently during the first half-cycle. No intermixing of components was found between TiO_2 and RuO_2. The temperature dependent measurements on TDMAT multilayer grown at room temperature, suggest that the heat was required to form the byproduct-imine species.

The present studies can contribute towards the improved understanding of the surface chemical processes which can lead to better protocols for growth of high quality thin films using CVD and ALD.

Acknowledgement

The work presented in this thesis resulted from the help and support of many people. I would, thus, like to utilize this opportunity to express my sincere indebtedness towards all of them.

Firstly, I thank my thesis supervisors **Joachim Schnadt, Lei Ye** and **Lars Montelius** for their inspiring guidance, analytical and critical suggestions. Special thanks to Joachim Schnadt and Lei Ye who have been patient bearers of my mistakes and always supported my efforts in this project. It is a great privilege to work under them, who motivated me in every course of my work and made me believe in myself. Whatever little I know about experimental physics, is all because of my main supervisor **Joachim Schnadt**.

I thank **Ashley R. Head** for being kind to hear my problems and several discussions during this thesis work. I am also thankful to **Tripta Kamra**, **Olesia Snezhkova**, **Niclas Johansson**, **Ashley R. Head**, **Sheetal Sisodya, Ekaterina Bolbat, and Payam Shayesteh** for their collaborations and participation in beamtimes, which cannot be as fun and fruitful in their absence. They all made a great working environment.

Xiantao Chen, Changgang Xu, Khan Mohammad Ahsan Uddin, Tongchang Zhou, and **Per-Olof Larsson** are acknowledged for sharing their experiences in chemical laboratories. Thanks to my officemate **Shabnam Oghbaiee**, for several discussions not only on academics but also on personal ground. Thanks to **Mohammad Alif Arman** for giving helping hand in STM laboratory.

I thanks to all the collaborators and co-authors. Special thanks to **Rocío Sánchez-de-Armas** and, **Barbara Brena** for DFT calculations.

I sincerely thank all former and present members of the Division of Synchrotron Radiation Research and Department of Pure and Applied Biochemistry for their discussions and amiable surroundings. I also thank people from Lund Nano Lab and the MAX-lab staff for their support. **Patrik Wirgin**, **Anneli Nilsson Ahlm** and **Ulla Jeppsson Wistrand** are acknowledged for taking care of all the non-scientific paper related work.

I also thank **Jneshwari**, **Sandeep Malik**, **Madhu**, **Priti Mohanty**, **Tania Singh**, **Vaibhav Diwan**, **Pallavi**, **Pintesh Lambhate, Sheetal and Ashish Yadav, Monika, Deepti, Rama, Srikanth Ranganathan** for their love and affection which helped me in staying positive during my stay in Skåne.

I thank my family members and friends for their affection and patience. It would not have been possible to complete this work without their loving support and blessings. I am forever indebted for the support and love received from my parents Gyan Singh Chaudhary and Vimlesh Chaudhary. In this sequence, my sisters Shikha, Priyanka, and brother Nitin, Nikhil are also acknowledged. I appreciate my in-laws, Susheela Kaptan Singh for being loving and caring, and Meena Vijendra

Singh and Mamata Rajendra Singh for always being generous. Words are incapable to thank Pushpendra P. Singh for standing by me all the time with encouraging and loving support. Last but not the least, I thank all those who remembered and wished me on every success.

Finally, I dedicate this thesis to **Almighty**.

References

[1] L. Bjaalie, B. Himmetoglu, L. Weston, A. Janotti, C. G. Van de Walle, Oxide interfaces for novel electronic applications, *New J. Phys. 16*, 025005 (2014).

[2] A. Ohtomo, H. Y. Hwang, A high-mobility electron gas at the $LaAlO_3/SrTiO_3$heterointerface, *Nature* 427, 423-426 (2004).

[3] M. Grätzel, Dye-sensitized solar cells, *J. Photochem. Photobiol.* C **4**, 145-153 (2003).

[4] B. O'Regan, M. Grätzel, A low-cost, high efficiency solar cell based on dye-sensitized colloidal TiO_2 films, *Nature* **353**, 737-740 (1991).

[5] I. Willner, B. Willner, Biomolecule-based nanomaterials and nanostructures, *Nano Lett.* **10**, 3805-3815 (2010).

[6] A. Kros, M. Gerritsen, V. S. I. Sprakel, N. A. J. M. Sommerdijk, J. A. Jansen, R. J. M. Nolte, Silica-based hybrid materails as biocompatible coatings for glucose sensors, *Sens. Actuators, B* **81**, 68-75 (2001).

[7] U. U. Díaz D. Brunelab, A. Corma, Catalysis using multifunctional organosiliceous hybrid materials, *Chem. Soc. Rev.***42**, 4083-4097 (2013).

[8] Q. Wu, L. Wang, Immobilization of copper(II) in organic-inorganic hybrid materials: A highly efficient and reusable catalyst for the classic Ullmann reaction, *Synthesis* **13,** 2007-2012 (2008).

[9] H. Y. Hwang, Y. Iwasa, M. Kawasaki,B. Keimer,N. Nagaosa , Y. Tokura, Emergent phenomena at oxide interfaces, *Nature Mater.* **11**, 103–113 (2012).

[10] K. Reimhult, K. Yoshimatsu, K. Risveden, S. Chen, L. Ye, A. Krozer, Characteriza-tion of QCM sensor surfaces coated with molecularly imprinted nanoparticles, *Biosens. Bioelectron.* **23**, 1908–1914 (2008).

[11] K. Haupt, K. Mosbach, Molecularly Imprinted Polymers and Their Use in Biomimetic Sensors, *Chem. Rev.* **100**, 2495–2504 (2000).

[12] J. Wackerlig, P. A. Lieberzeit, Molecularly imprinted polymer nanoparticles in chemical sensing – Synthesis, characterisation and application, *Sens. Actuators. B* **207**, 144–157 (2015).

[13] B. Sellergren, C.J. Allender, Molecularly imprinted polymers: A bridge to advanced drug delivery, *Adv. Drug Delivery Rev.* **57**, 1733 – 1741 (2005).

[14] A.G. Mayes a , M.J. Whitcombe Synthetic strategies for the generation of molecularly imprinted organic polymers, *Adv. Drug Delivery Rev.* **57**, 1742 – 1778 (2005).

[15] M. Valden, X. Lai, and D.W. Goodman, Onset of catalytic activity of gold clusters on titania with the appearance of nonmetallic properties, *Science* **281**, 1647-1650 (1998).

[16] C. T. Campbell, The Energetics of Supported Metal Nanoparticles: Relationships to Sintering Rates and Catalytic Activity, *Acc. Chem. Res.* **46**, 1712–1719 (2013).

[17] M. Haruta, N. Yamada, T. Kobayashi, S. Iijima, Gold catalysts prepared by coprecipitation for low-temperature oxidation of hydrogen and of carbon monoxide, J. *Catal.* **115**, 301 (1989).

[18] J. W. Klaus, O. Sneh, and S. M. George, Growth of SiO_2 at Room Temperature with the Use of Catalyzed Sequential Half-Reactions, *Science* **278**, 1934 (1997).

[19] J. Bachmann, R. Zierold, Y.T. Chong, R. Hauert, C.Sturm, R. S.-Grund, B. Rheinlnder, M. Grundmann, U. Gösele, K. Nielsch, A Practical, Self-Catalytic, Atomic Layer Deposition of Silicon Dioxide, *Angew. Chem. Int. Ed.* **47**, 6177 –6179 (2008).

[20] T. T. U. Le, A. Sasahara, M. Tomitori, Water Wettability of an Ultrathin Layer of Silicon Oxide Epitaxially Grown on a Rutile Titanium Dioxide (110) Surface, *Phys. Chem. C* **117**, 23621−23625 (2013).

[21] T. A. Jurgens-Kowal , J. W. Rogers, Jr., Pyrolysis of Tetraethoxysilane on Mo(100) at Low Temperatures, *J. Phys. Chem. B* **102**, 2193-2206 (1998),

[22] K. L. Choy, Chemical vapour deposition of coatings, *Prog. Mater. Sci.* **48,** 57–170 (2003)

[23]D. A. P. Bulla, N.I. Morimoto, Deposition of thick TEOS PECVD silicon oxide for integrated optical wave guide applications, *Thin Solid Films* **334**, 60-64 (1998).

[24] J. E. Crowell, L. L. Tedder, H.-C. Cho, F. M. Cascarano, M. A. Logan, Model studies of dielectric thin film growth: Chemical vapor deposition of SiO_2, *J. Vac. Sci. Technol. A* **8**, 1864-1870 (1990).

[25] N. M. Suárez, G. Palmisano, L. M. Ferrer, C. M.Gutiérrez, S. Yurdakal, V. Augugliaro, M. Pagliaro, D.F. Monte, Self-assembled titania–silica–sepiolite based nanocomposites for water decontamination, *J. Mater. Chem.* **19**, 2070-2075 (2009).

[26] S. M. George, Atomic Layer Deposition: An Overview, *Chem. Rev.* **110**, 111–131(2010).

[27] S. K. Kim, W. D. Kim, K. M. Kim, C. S. Hwang, J. Jeong, High dielectric constant TiO_2 thin films on a Ru electrode grown at 250 °C by atomic-layer deposition, J. *Appl. Phys. Lett.* **85**, 4112-4114 (2004).

[28] K. Fröhlich, J. Aarik, M. Ťapajna, A. Rosová, A. Aidla, E. Dobročka, K. J. Hušková, Epitaxial growth of high- κ TiO_2 rutile films on RuO_2 electrodes, *Vac. Sci. Technol. B*, **27**, 266-270 (2009).

[29] A. Einstein, Über einen die Erzeugung und Verwandlung des Lichtes betreffenden heuristischen Gesichtspunkt, *Ann. Phys.* **17**,132-148 (1905).*(English translation at* http://dx.doi.org/2010.1119/1.1971542*).*

[30] K. Siegbahn, Electron spectroscopy for atoms, molecules and condensed matter, Nobel lecture (1981), http://www.nobelprize.org.

[31] See, e.g., S. Hüfner, Photoelectron Spectroscopy: Principles and Applications, 3rd Edition, *Springer*, Berlin, Heidelberg (2003).

[32] J. N. Andersen, D. Hennig, E. Lundgren, M. Methfessel, R.Nyholm, M. Scheffler, Surface core-level shifts of some 4*d*-metal single-crystal surfaces: Experiments and *ab initio* calculations, *Phys. Rev. B* ***50***, 17525 (1994).

[33] R.T. Poole, R. C. G. Leckey, J. G. Jenkin, J. Liesegang, Calibration procedures for photoelectron spectrometers, *J. Phys. E* **6**, 201-203 (1973).

[34] R. Manne and T. Åberg, Koopmans' theorem for inner-shell ionization, *Chem. Phys. Lett.***7**,282-284 (1982).

[35] G. Attard and C. Barnes, Surfaces, *Oxford University Press*, Oxford (2009).

[36] A. Jablonski, C. J. Powell, Relationships between electron inelastic mean free paths, effective attenuation lengths, and mean escape depths, *J. Electron. Spectrosc. Relat. Phenom.* **100**, 137-160 (1999).

[37] A. Jablonski, Effects of Auger electron elastic scattering in quantitative AES, *Surf. Sci.* **188**, 164-180 (1987).

[38] D. Roy, D. Tremblay, Design of electron spectrometers, *Rep. Prog. Phys.* **53**, 1621-1674 (1990).

[39] See, e.g., M. Wiklund, A. Beutler, R. Nyholm, J. N. Andersen, Vibrational analysis of the C 1s photoemission spectra from pure ethylidyne and ethylidyne coadsorbed with carbon monoxide on Rh(111), *Surf. Sci.* **461**, 107-117 (2000).

[40] M. Coville, T. D. Thomas, Molecular effects on inner-shell lifetimes: Possible test of the one-center model of Auger decay, *Phys. Rev. A* **43**, 6053-6056 (1991).

[41] L. Österlund, P. B. Rasmussen, P. Thostrup, E. Lægsgaard, I. Stensgaard, and F. Besenbacher, Bridging the Pressure Gap in Surface Science at the Atomic Level: *H*/Cu(110), *Phys. Rev. Lett.* **86**, 460 (2001).

[42] J. A. Jensen, K. B. Rider, M. Salmeron, G. A. Somorjai, High Pressure Adsorbate Structures Studied by Scanning Tunneling Microscopy: CO on Pt(111) in Equilibrium with the Gas Phase, *Phys. Rev. Lett.* **80**,1228 (1998).

[43] K. B. Rider, K. S. Hwang, M. Salmeron, and G. A. Somorjai, Structure and Dynamics of Dense Monolayers of NO Adsorbed on Rh(111) in Equilibrium with the Gas Phase in the Torr Pressure Range, *Phys. Rev. Lett.* **86**, 4330(2001).

[44] M. Salmeron, R. Schlögl, Ambient pressure photoelectron spectroscopy: A new tool for surface science and nanotechnology, *Surf. Sci. Rep*. **63**, 169–199 (2008).

[45] J. Schnadt, J. Knudsen, J. N. Andersen, H. Siegbahn, A. Pietzsch, F. Hennies, N. Johansson, N. Mårtensson, G. Öhrwall, S. Bahr, S. Mähl, O. Schaff, The New Ambient Pressure X-ray Photoelectron Spectroscopy Instrument at MAX-lab, *J. Synchrotron Rad.* **19**, 701-704 (2012).

[46] Niclas Johansson. The HPXPS Instrument at Max-lab: A Powerful Tool for in situ Catalysis Investigations. M.Sc. Thesis, Lund University (2012).

[47] G. Binning, H. Rohrer, C. Gerber, E. Weibel, Surface Studies by Scanning Tunneling Microscopy, *Phys. Rev. Lett.* **49**, 57 (1982).

[48] http://nobelprize.org/nobel_prizes/physics/laureates/1986/

[49] http://nobelprize.org/nobel_prizes/physics/laureates/1986/rohrer-lecture.pdf

[50] G. Binning, H. Rohrer, C. Gerber, E. Weibel, Surface Studies by Scanning Tunneling Microscopy, *Phys. Rev. Lett*. **49**, 57 (1982).

[51] J. Tersoff, D. R. Hamann, Theory of the scanning tunneling microscope, *Phys. Rev. B* **31**, 85 (1985).

[52] J. Bardeen, Tunneling from a many-particle point of view, *Phys. Rev. Lett*. **6**, 57 (1961).

[53] C. J. Chen, Introduction to Scanning Tunneling Microscopy, *Oxford University Press*, New York (2007), Chapter 9.

[54] C. J. Chen, Introduction to Scanning Tunneling Microscopy, *Oxford University Press*, New York (2007), Chapter 1.

[55] F. J. Green, Sigma-Aldrich Handbook of Stains, Dyes and Indicators, *Aldrich Chemical Company, Inc.*, Milwaukee, Wisconsin (1990).

[56] J. Goldstein, D. E. Newbury, D. C. Joy, C. E. Lyman, P. Echlin, E. Lifshin, *L. Sawyer, J. R. Michael,* Scanning Electron Microscopy and X-ray Microanalysis, 3rd edition, *Plenum*, New York, (2003).

[57] G. Binnig, C. F. Quate, Atomic Force Microscope *Phys. Rev. Lett.* **56**, 930 (1986).

[58] J. Y. Tseng, M. H. Lin, L. K. Chau, Preparation of colloidal gold multilayers with 3-(mercaptopropyl)-trimethoxysilane as a linker molecule, *Colloids Surf., A* **182**, 239–245 (2001).

[59] R. P. Pogorilyi, I. V. Melnyk, Y. L. Zub, G. A. Seisenbaeva, V. G. Kessler Immobilization of urease on magnetic nanoparticles coated by polysiloxane layers bearing thiol- or thiol- and alkyl-functions, *J. Mater. Chem. B* **2**, 2694–2702 (2014).

[60] G. L. Witucki, A Silane Primer: Chemistry and Applications of Alkoxy Silanes, *J. Coat.Technol.* **65**, 57-60 (1993).

[61] N. Aissaoui, L. Bergaoui, J. Landoulsi, J.-F. Lambert, S. Boujday, Silane Layers on Silicon Surfaces: Mechanism of Interaction, Stability,and Influence on Protein Adsorption, *Langmuir* **28**, 656-665 (2012).

[62] L.-S. jang, H.-J. Liu, Fabrication of protein chips based on 3-aminopropyltriethoxysilane as a monolayer, *Biomed. Microdevices* **11**, 331-338 (2009).

[63] S. K. Vashist, E. Lam, S. Hrapovic, K. B. Male, J. H. T. Luong, Immobilization of Antibodies and Enzymes on 3-Aminopropyltriethoxysilane-Functionalized Bioanalytical Platforms for Biosensors and Diagnostics, *Chem. Rev.* **114**, 11083−11130 (2014).

[64] K. L. Son, S. H. Ahn, J. H. Kim, W. G. Koh, Graft Copolymer-Templated Mesoporous TiO_2 Films Micropatterned with Poly(ethylene glycol) Hydrogel: Novel Platform for Highly Sensitive Protein Microarrays. *ACS Appl. Mater. Interf.* **3**, 573–581 (2011).

[65] H. Wang, Y. Zhang, X. Yuan, Y. Chen, M. Yan, A universal protocol for photochemical covalent immobilization of intact carbohydrates for the preparation of carbohydrate microarrays, *Bioconjugate Chem.* **22**, 26–32 (2011).

[66] K. Yoshimatsu, L. Ye, P. Stenlund, I.S. Chronakis, A simple method for preparation of molecularly imprinted nanofiber materials with signal transduction ability, *Chem. Commun.***17**, 2022-2024 (2008).

[67] S. Hajizadeh, C. Xu, H. Kirsebom, L. Ye, B. Mattiasson, Cryogelation of molecularly imprinted nanoparticles: A macroporous structure as affinity chromatography column for removal of β-blockers from complex samples, *J. Chromatogr. A* **1274**, 6–12 (2013).

[68] J.P. Spatz, S. Mössmer, C. Hartmann, M. Möller, T. Herzog, M. Krieger, H.-G. Boyen, P. Ziemann, and B. Kabius, *Langmuir* **16**, 407 (2000).

[69] U. Diebold, The surface science of titanium dioxide, *Surf. Sci. Rep.* **48**, 53-229 (2003).

[70] M. Ramamoorthy, D. Vanderbilt, R. D. King-Smith, First-principles calculations of the energetics of stoichiometric TiO_2 surfaces, *Phys. Rev. B* **49**, 16721-16727 (1994).

[71] W. Göpel, J.A. Anderson, D. Frankel, M. Jaehnig, K. Phillips, J.A. Schäfer, G. Rocker, Surface defects of TiO_2(110): A combined XPS, XAES and ELS study, *Surf. Sci.* **139**, 335-346 (1984).

[72] S. Wendt, P. T. Sprunger, E. Lira, G. K. H. Madsen, Z. Li, J. Ø. Hansen, J. Matthiesen, A. Blekinge-Rasmussen,E. Lægsgaard, B. Hammer, F. Besenbacher, The Role of Interstitial Sites in the Ti3d Defect State in the Band Gap of Titania, *Science* **320**, 1755-1759 (2008).

[73] S. Wendt, R. Bechstein, S. Porsgaard, E. Lira, J. Ø. Hansen, P. Huo, Z. Li, B. Hammer, F. Besenbacher, Comment on "Oxygen Vacancy Origin of the Surface Band-Gap State of TiO_2(110)", *Phys. Rev. Lett.* **104**, 259703 (2010).

[74] Z. Zhang, J. Lee, J. T. Yates Jr., R. Bechstein, E. Lira, J. Ø. Hansen, S. Wendt, F. Besenbacher, Unraveling the Diffusion of Bulk Ti Interstitials in Rutile TiO_2(110) by Monitoring Their Reaction with O Adatoms, *J. Phys.Chem.* C **114**, 3059-3062 (2010).

[75] N. G. Petrik, Z. Zhang, Y. Du, Z. Dohnlek, I. Lyubinetsky, G. A. Kimmel, Chemical Reactivity of Reduced TiO_2(110): The Dominant Role of Surface Defects in Oxygen Chemisorption, *J. Phys. Chem.* C **113**, 12407-12411 (2009).

[76] C. M. Yim, C. L. Pang, G. Thornton, Oxygen Vacancy Origin of the Surface Band-Gap State of TiO_2(110), *Phys. Rev. Lett.* **104**, 036806 (2010).

[77] C. M. Yim, C. L. Pang, G. Thornton, A Reply to the Comment by S. Wendt et al., *Phys. Rev. Lett.* **104**, 259704 (2010).

[78] H. Over, Surface Chemistry of Ruthenium Dioxide in Heterogeneous Catalysis and Electrocatalysis: From Fundamental to Applied Research, *Chem. Rev.* ***112***, 3356 (2012).

[79] Y. Wei, U. Martinez, L. Lammich, F. Besenbacher, S.Wendt, Formation of metastable, heterolytic H-pairs on the RuO2(110) surface, *S. Surf. Sci.* **619**, L1-L5 (2014).

[80] J.-O. Carlsson, U. Jansson, Progress in Chemical Vapor Deposition, *Prog. Solid St. Chem.* **22**, 237-292 (1993).

[81] S. M. George, Atomic Layer Deposition: An Overview, *Chem. Rev.* **110**, 111–131 (2010).

[82] S. J. Gaskell, Electrospray: Principles and Practice, *J. Mass Spectrom.* **32**, 677-688 (1997).

[83] C. J. Satterley, L.M.A. Perdigão, A. Saywell, G. Magnano, A. Rienzo, L.C. Mayor, V.R. Dhanak, P.H. Beton, and J.N. O'Shea, Electrospray deposition of fullerenes in ultra-high vacuum:in situ scanning tunneling microscopy and photoemission spectroscopy, *Nanotechnology* **18**, 455304 (2007).

[84] J. A. Howarter, J. P. Youngblood, Optimization of silica Silanization by 3-Aminopropyltriethoxysilane, *Langmuir* **22**, 11142-11147 (2006).

[85] N.-Y Cui, C. Liu, W. Yang, XPS and AFM characterization of the self-assembled molecular monolayers of a 3-aminopropyltrimethoxysilane on silicon surface, and effects of substrate pretreatment by UV-irradiation, *Surf. Interface Anal.* **43**, 1082–1088 (2010).

[86] T. Dubrovsky, A. Tronin, S. Dubrovskaya, S. Vakula, C. Nicolini, Immunological activity of IgG Langmuir films oriented by protein A sublayer, *Sens. Actuators B* **23**, 1-7 (1995).

[87] M. S. Islam, H. Yu, H. G. Lee, S. H. Kang, Molecular switching fluorescence based high sensitive detection of label-free C-reactive protein on biochip, *Biosens. Bioelectron.* **26**, 1028-1035 (2010).

[88] Gamble, L.; Jung, L. S.; Campbell, C. T. Interaction of Silane Coupling Agents with the TiO_2(110) Surface. *Langmuir*, **1995**, *11*, 4505-4514.

[89] L. Gamble, M. B. Hugenschmidt, C. T. Campbell, Teresa A. Jurgens, and J. W. Rogers, Jr. Adsorption and Reactions of Tetraethoxysilane (TEOS) on Clean and Water-Dosed Titanium Dioxide (110), *J. Am. Chem. Soc*. **115**, 12096-12105 (1993).

[90] Pabon, E.;Jaime Retuert, J.; Quijada, R.; Zarate, A., TiO_2–SiO_2 Mixed Oxides Prepared by a Combined Sol–gel and Polymer Inclusion Method. *Micropor. Mesopor. Mater.* **67**, 195–203 (2004.)

[91] D. Sun, Y. Huang, B. Han, G. Yang, Ti-Si Mixed Oxides Prepared by Polymer in Situ Sol-Gel Chemistry with the Aid of CO_2. *Langmuir* **22**, 4793-4798 (2006).

[92] N. A.Dahoudia, J. Xia, G. Caoa, Silica modification of titania nanoparticles for a dye-sensitized solar cell, *Electrochim. Acta* **59**, 32– 38 (2012).